JOURNAL OF GEOPHYSICAL RESEARCH: SOLID EARTH, VOL. 118, 878–896, doi:10.1002/jgrb.50106, 2013

Numerical investigation of the interplay between wall geometry and friction in granular fault gouge

Andrew P. Rathbun,[1] François Renard,[1,2] and Steffen Abe[3]

Received 20 July 2012; revised 2 December 2012; accepted 23 January 2013; published 27 March 2013.

[1] The influence of surface roughness is central in understanding the behavior of various types of shear zones including faults, landslides, and deformation in glacial till. All of these systems contain a non-planar rough wall, which interacts with either a gouge zone or another wall. We use the 3-D discrete element method (DEM) to investigate both the effect of boundary roughness and friction. Granular non-cohesive gouge is sandwiched between rough walls with large grooves, or smooth walls composed of spherical particles that can be adjusted to control roughness. Roughness and gouge properties are scaled to laboratory friction experiments. We vary friction between the particles and the wall and monitor shear strength, height, coordination number, distribution, and orientation of particle forces, localization, and porosity distribution in the shear zone. We find that, on the first-order, strength is controlled by particle-particle friction and mechanical coupling of the fault zone wall to the gouge. Rough boundaries (RMS roughness > grain radius) force more shear within the gouge zone, dilating the layer and sliding more grains, which leads to large stress necessary to shear the layer. When large amplitude roughness is removed, and roughness is at the grain-scale, the coupling, and thus the strength, is controlled by both wall and particle friction as well as fine-scale boundary roughness. These differences are reflected in profiles of shear within the gouge zone and offset at the boundary in smooth models. From our simulations, we quantify how and why rough natural faults will have a higher overall strength.

Citation: Rathbun, A. P., F. Renard, and S. Abe (2013), Numerical investigation of the interplay between wall geometry and friction in granular fault gouge, *J. Geophys. Res. Solid Earth*, *118*, 878–896, doi:10.1002/jgrb.50106.

1. Introduction

[2] Natural fault zones are rough, non-planar features with spatial variations of their topography ranging from microns to hundreds of kilometers both along and perpendicular to slip. This roughness has been measured on exhumed fault surfaces that have recorded shear processes near the surface [*Power et al.*, 1987, 1988; *Renard et al.*, 2006; *Sagy et al.*, 2007; *Candela et al.*, 2009], or at depth [*Bistacchi et al.*, 2011]. Roughness can also be measured on the basal surface of glaciers [*Nye*, 1969; *Kamb*, 1970; *Ross et al.*, 2012] and landslides [*Legros*, 2002; *Gee et al.*, 2005; *Davies et al.*, 2006; 2010].

[3] A granular layer derived from mechanical and chemical process in shearing layers is often observed in landslides, beneath glaciers and in faults. Examinations of both exhumed fault zones [e.g., *Sibson*, 1977; *Logan et al.*, 1979; *Chester et al.*, 1985; *Chester and Chester*, 1998; *Chester and Logan*, 1986; *Cashman and Cashman*, 2000; *Faulkner et al.*, 2003; *Hayman et al.*, 2004; *Cashman et al.*, 2007] and faults at depth [*Heermance et al.*, 2003; *Boullier et al.*, 2004; *Zoback*, *et al.*, 2010] show the presence of a gouge zone that collects the wear particles produced by friction processes. A similar layer is observed under many glaciers. Due to limitations of the strain rate of ice in creep, fast motion of ice streams and glaciers is the result of either sliding of the glacier over its bed or shear within the frictional granular-till layer beneath the ice, making the till-ice system analogous to faults [*Kamb*, 2001; *Cuffy and Patterson*, 2010].

[4] The role of fault zone roughness in both fault zone strength and seismic slip is still debated. At the atomic scale, asperity contacts have been shown to control friction [*Bowden and Tabor*, 1950] and stick-slip motion [*Persson*, 2000]. At the fault scale, *Candela et al*. [2011a; 2011b] proposed that roughness variations could control the stress drop and slip distribution during earthquakes. The effect of fault roughness on the heterogeneity of stress distribution and sliding resistance within the fault zone has been investigated by numerical means [*Saucier et al.*, 1992; *Chester and Chester*, 2000; *Dieterich and Smith*, 2009; *Angheluta et al.*, 2011].

[5] Fault zone roughness has been theorized to control fault zone strength at depth and rupture of earthquakes

[1]ISTerre-Institut des Sciences de la Terre, Université of Grenoble 1 and CNRS, Grenoble, France.
[2]PGP, Physics of Geological Processes, University of Oslo, Oslo, Norway.
[3]Geologie-Enogene Dynamik, RWTH Aachen University, Aachen, Germany.

Corresponding author: A. P. Rathbun, ISTerre-Institut des Sciences de la Terre, Université of Grenoble 1 and CNRS, BP 53, 38041 Grenoble France. (andrew.rathbun@ujf-grenoble.fr)

2169-9313/13/10.1002/jgrb.50106

[e.g., *Pechmann and Kanamori*, 1982; *Sibson*, 1984] and variability in source parameters [e.g., *Venkataraman and Kanamori*, 2004; *Choy and Kirby*, 2004; *Schmittbuhl et al*., 2006]. Discrete element models in 2-D have shown that roughness controls the local stresses and thus slip style, e.g., stick-slip versus creep [*Fournier and Morgan*, 2012]. It has also been proposed that the roughness of fault planes could control the velocity of rupture propagation, with smoother fault showing supershear ruptures [*Bouchon et al*., 2010]. Roughness controlling slip style has been observed in laboratory experiments where smooth interfaces were used to produce supershear ruptures [*Rosakis et al*., 1999; *Xia et al*., 2004; *Schubnel et al*., 2011].

[6] Laboratory experiments on simulated faults and gouge zones have shown that roughness influences the strength and also the localization state, which in turn helps control frictional stability [e.g., *Dieterich*, 1981; *Biegel et al*., 1989; *Marone et al*., 1990; 1992; *Anthony and Marone*, 2005]. A rough fault zone promotes the distribution of shear into the layer and velocity-strengthening frictional behavior until shear is localized and there is a transition to velocity weakening [*Biegel et al*., 1989; *Marone et al*., 1990; *Beeler et al*., 1996], even though some experiments have shown that localization can occur in a velocity-strengthening sample [*Rathbun and Marone*, 2010]. Laboratory studies on the difference between rough and smooth fault boundaries have been interpreted using granular models in two dimensions showing that roughness controls the thickness of the active zone and grain bridges or force chains [*Mühlhaus and Vardoulakis*, 1987; *Sammis and Steacy*, 1994]. However, understanding the conditions that control localization and the interaction between the fault zone walls and the gouge are still incomplete, particularly in three dimensions.

[7] In the present study, we investigate the role of fault zone roughness on the strength of the gouge with fully three-dimensional, granular discrete element numerical simulations. The numerical model is calibrated using published laboratory data of the frictional strength of granular shear zones. Due to the inherently discontinuous nature of gouge zones in brittle shear, we choose to use the discrete elements method (DEM) due to the lack of dependence on a meshing system and grid.

[8] While no model is capable of capturing all the behavior of a natural system, the DEM is an accepted method of investigating granular flow in physics and fluid dynamics [see *Allen and Tildesley*, 1987; *Pöschel and Schwager*, 2005; *Radjaï and Dubois*, 2011 for recent reviews of the method]. DEM has been used into investigations of numerous geologic and geophysical studies [e.g., *Saltzer and Pollard*, 1992; *Mora and Place*, 1994; 1998; *Antonellini and Pollard*, 1995; *Aharonov and Sparks*, 1999; *Morgan and Boettcher*, 1999; *Burbridge and Braun*, 2002; *Finch et al*., 2003; *Morgan and McGovern*, 2005a, 2005b; *Abe and Mair*, 2009; *Goren et al*., 2011; *Fournier and Morgan*, 2012]. DEM has been shown to agree with laboratory experiments of sand piles [e.g., *Morgan and McGovern*, 2005a] granular experiments in two [e.g., *Knuth and Marone*, 2007; *Kruyt*, 2003; *Roux and Chevior*, 2011] and three dimensions [e.g., *Silbert et al*., 2002a, 2002b; *Abe and Mair*, 2009].

[9] In our models, fault zone roughness is varied from amplitude much larger than the grain scale to below the grain scale. Additionally we investigate the role of contrasting the frictional properties of granular shear zone with shear zone boundaries to simulate a shear zone made of weak walls (serpentinite, ice, clay, etc.), strong walls (quartzo-feldspathic minerals, etc.), and walls and gouge composed of the same material. In all models, we measure the frictional shear strength, shear zone thickness, porosity across the shearing layer, number of locked and sliding contacts, distribution of shear, distribution of particle-particle force, and orientation of contact and force vectors. The goals of the study are to answer the following questions:

[10] 1. What is the effect of fault roughness on the overall strength of the gouge?

[11] 2. How does this strength depend on the frictional properties of individual grains and the contrast of frictional properties between the fault wall and the gouge?

[12] 3. How is shear partitioned between sliding at the fault/gouge interface and distribution of granular shear within the gouge?

2. Methods

2.1. Numerical Method

[13] To model the role of boundary roughness on the shear of granular gouge, we employ the discrete element method (DEM) [*Cundall and Strack*, 1979; *Mora and Place*, 1994; *Place and Mora*, 1999]. All models are conducted with the open source, three-dimensional DEM simulation package ESyS-Particle [*Abe et al*., 2003] (https://launchpad.net/esys-particle/).

[14] In the model, spherical particles interact with their nearest neighbors through frictional and brittle-elastic interactions. Each particle is governed by using its radius, mass, position, and linear and angular velocity. Particles carry mass and kinetic energy and when two particles are in contact, they are repelled based on elastic forces (i.e., Hooke's law) and slide based on a linear Coulomb friction law, with the friction coefficient at particle-particle contacts, $\mu_{particle}$, varied between runs. Particles can be bonded together using elastic brittle bonds to form aggregate solid masses such as fault zone boundaries. Bond parameters are chosen so that solid blocks behave as a linear elastic solid [*Wang et al*., 2006]. More details on the Lattice-Solid Model and its extension, ESyS-Particle can be found in *Mora and Place* [1994, 1998], *Abe et al*. [2003], and *Wang et al*. [2006].

2.2. Model Properties

[15] In all models we use a granular shear zone of length (l_x), 60 model units, initial thickness of the shearing layer 30 model units (l_y), and depth of 18 model units (l_z) (Figure 1). The model is periodic in the x dimension allowing gouge particles (red grains in Figure 1) and the moving wall to exit one side and re-enter on the opposite side during shear. In the front and back, two frictionless walls contain the gouge. Shear zone walls (blue grains in Figure 1) are constructed from bonded particles. To isolate the role of geometry and particle friction, the bonds are not allowed to break. Gouge particles range from 0.5 to 1.0 model units in radius with the grain size distribution governed by a power law of exponent −4.7 from 0.5 to 0.8 and then the number of grains is constant until 1.0 (Figure 1c). The model geometry is filled with a dense packing

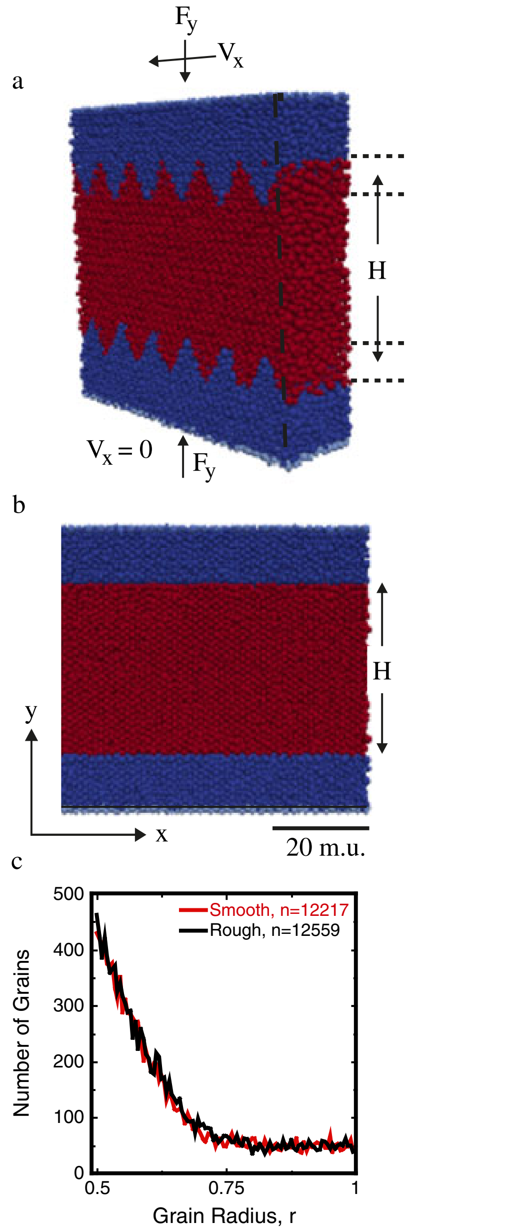

Figure 1. (a and b) Three-dimensional discrete element models are constructed from spherical particles, which are bonded together to form fault walls (blue). The gouge zone (red) consists of ~12,000 unbounded spheres, for Figure 1a $R_{\mathrm{RMS}} = 2.4$ with large amplitude grooves and Figure 1b $R_{\mathrm{RMS}} = 0.58$. H is given as the distance between the groove mid-line in Figure 1a and the walls in Figure 2b. Force (F_y) is applied equally in the normal direction to the top and bottom walls, which are both allowed to freely move in the y direction. Shear velocity, V_x is applied to the top wall, while the bottom is held stationary. (c) Power law grain size distribution for smooth and rough models. Length units are given in terms of maximum particle radius.

of grains where each particle contacts at least four surrounding grains using the algorithm of *Place and Mora* [2001].

[16] Models are sheared at a constant rate, $V_x = 10^{-3}$ model units, a similar shear rate to other DEM simulations of granular gouge [*Aharonov and Sparks*, 2002; *Mair and Abe*, 2008; *Abe and Mair*, 2009] corresponding to several meters per second. We cast velocity into inertial number, I:

$$I = \frac{m\dot{\gamma}^2}{P} \tag{1}$$

where m is the particle mass, $\dot{\gamma}$ is the strain rate of the active layer, and P is confining pressure, which can be taken to be normal stress [*Midi*, 2004; *da Cruz et al.*, 2005; *Koval et al.*, 2009; *Shojaaee et al.*, 2012a]. This allows our simulations to be directly compared to other DEM work.

[17] At $I \gg 1$the model behaves as a granular gas and is dominated by grain-grain collisions and inertial effects, while at $I \ll 1$ the model is quasi-static with force chains created and destroyed at equal rates. Taking an active layer of ~7 model units (see section 3.2), our main suite of simulations are conducted at $I \approx 4 \times 10^{-3}$. We check these results by running select simulations at $I \approx 2 \times 10^{-4}$ and $I \approx 4 \times 10^{-5}$. A large shear velocity is necessary in DEM simulations to decrease computing time while maintaining large shear strain. Reducing V_x by a factor of 5 and 10 ($I \approx 2 \times 10^{-4}$ and $I \approx 4 \times 10^{-5}$) produces similar results. For complete discussion of the role of I, we refer to *da Cruz et al.* [2005] and *Shojaaee et al.* [2012a] and references therein.

[18] We explore the role of boundary roughness and frictional properties on macroscopic and microscopic properties of the shear zone. To investigate the boundary roughness, experiments are conducted with the fault zone walls constructed from particles ranging from 0.4 to 1.0 model units in radius following the distribution presented in Figure 1c to produce boundaries that are rough on the grain-scale. Additionally, some experiments contain large-scale "saw-tooth" roughness made of the wall particles to promote shear within the gouge and simulate a rough fault (Figures 1a and 1b). The amplitude of the saw tooth is chosen such that the numerical simulations could be compared to the laboratory experiments of *Mair et al.* [2002], *Frye and Marone* [2002], *Anthony and Marone* [2005], and *Fulton and Rathbun* [2011]. Due to the presence or absence of grooves, the total height varies between our geometries, but in all cases the thickness of the gouge, H, is the same at the start of the experiment. In models with the saw-tooth boundary, the layer thickness is calculated from the tooth centers (Figure 1a). Keeping the initial H constant for all models ensures that the number of gouge particles, n, is nearly constant which allows for comparison of steady state H, sliding contacts, locked contacts and other parameters between models and roughness.

[19] To isolate the role of boundary roughness on macroscopic shear strength and how roughness changes microscopic properties such as fabric and particle-particle force, we do not allow the evolution of roughness and thus, the fault zone walls are not allowed to break. In nature, this condition is not always met, as cumulative slip tends to erode the fault walls. But other processes, such as crack branching or wear, create roughness, such that the walls of fault zones observed on the field always display some morphological corrugations.

[20] To investigate the role of roughness on fault strength, we vary μ at particle-particle contacts (μ_{particle}) and particle-wall contacts (μ_{wall}); see Table 1 for complete list of μ and roughness conditions for each model. We explore roughness thresholds by constructing the walls with particles smaller than the gouge with the minimum grain radius, r_{min}, equal to 0.4 and then decreasing r_{min} by two-fold, and four-fold

Table 1. Numerical Experiment Table[a]

Name	Roughness, RMS	Wall μ	Particle μ	⟨μ_{macro}⟩	⟨H⟩
g282	2.4	0.1	0.1	0.303 ± 0.009	23.492 ± 0.021
g284	2.4	0.01	0.01	0.261 ± 0.010	22.857 ± 0.019
g285	2.4	0.2	0.2	0.356 ± 0.011	24.018 ± 0.018
g286	2.4	0.3	0.3	0.380 ± 0.014	24.324 ± 0.043
g287	2.4	0.4	0.4	0.404 ± 0.016	24.638 ± 0.072
g288	2.4	0.5	0.5	0.424 ± 0.010	24.804 ± 0.060
g289	2.4	0.6	0.6	0.432 ± 0.015	24.958 ± 0.061
g290	2.4	0.7	0.7	0.439 ± 0.019	25.084 ± 0.072
g291	2.4	0.8	0.8	0.448 ± 0.015	25.191 ± 0.070
g292	2.4	0.9	0.9	0.458 ± 0.019	25.223 ± 0.084
g293	2.4	1	1	0.454 ± 0.018	25.296 ± 0.081
g319	2.4	0.5	0.5	0.348 ± 0.011	24.061 ± 0.060
g320	0.58	0.1	0.5	0.317 ± 0.016	23.913 ± 0.051
g321	2.4	0.1	0.5	0.418 ± 0.013	24.613 ± 0.050
g351	0.58	0.1	0.1	0.277 ± 0.010	22.928 ± 0.013
g352	0.58	0.3	0.3	0.333 ± 0.012	23.668 ± 0.034
g353	0.58	0.01	0.01	0.201 ± 0.010	22.307 ± 0.025
g358	0.58	0.1	0.3	0.318 ± 0.013	23.588 ± 0.044
g359	0.58	0.5	0.1	0.281 ± 0.010	22.928 ± 0.019
g360	0.58	0.1	0.01	0.197 ± 0.011	22.314 ± 0.029
g361	0.58	0.5	0.3	0.344 ± 0.011	23.684 ± 0.031
g362	0.58	0.5	0.01	0.200 ± 0.010	22.323 ± 0.025
g363	2.4	0.1	0.3	0.382 ± 0.009	24.213 ± 0.051
g364	2.4	0.1	0.01	0.259 ± 0.010	22.883 ± 0.019
g365	2.4	0.5	0.3	0.384 ± 0.014	24.364 ± 0.039
g366	2.4	0.5	0.01	0.258 ± 0.009	22.893 ± 0.025
g367	2.4	0.1	0.8	0.451 ± 0.017	24.918 ± 0.056
g368	2.4	0.5	0.8	0.444 ± 0.015	25.133 ± 0.074
g369	0.58	0.1	0.8	0.307 ± 0.018	24.179 ± 0.080
g370	0.58	0.1	0.8	0.307 ± 0.018	24.179 ± 0.080
g371	0.58	0.5	0.8	0.357 ± 0.017	24.370 ± 0.062
g372	0.58	0.8	0.8	0.360 ± 0.017	24.379 ± 0.055
g373	0.58	0.5	1	0.352 ± 0.016	24.483 ± 0.079
g374	0.58	0.1	1	0.303 ± 0.019	24.271 ± 0.074
g375	0.58	1	1	0.381 ± 0.019	24.550 ± 0.059
g376_a	0.58	0.5	0.5	0.348 ± 0.011	24.076 ± 0.048
g376_b	0.58	0.5	0.5	0.348 ± 0.011	24.076 ± 0.048
g377	2.4	0.5	0.1	0.299 ± 0.011	23.548 ± 0.030
g378	2.4	0.5	0.8	0.457 ± 0.018	25.281 ± 0.069
g379	2.4	0.1	1	0.459 ± 0.019	25.013 ± 0.073
g380	0.58	0.1	0.1	0.277 ± 0.010	22.928 ± 0.013
g381	0.58	0.5	0.5	0.347 ± 0.011	24.061 ± 0.060
g382	2.4	0.5	0.5	0.425 ± 0.010	24.804 ± 0.056
g383	2.4	0.5	0.5	0.420 ± 0.014	24.803 ± 0.053
g384	0.35	0.5	0.5	0.296 ± 0.013	24.284 ± 0.061
g385	0.13	0.5	0.5	0.250 ± 0.013	24.414 ± 0.054
g426	0.35	0.2	0.2	0.270 ± 0.011	26.242 ± 0.026
g427	0.13	0.2	0.2	0.235 ± 0.008	23.713 ± 0.029
g433[b]	2.4	0.5	0.5	0.349 ± 0.012	24.047 ± 0.041
g469[d]	0.58	0.5	0.5	0.363 ± 0.014	23.900 ± 0.065
g470	0.13	0.2	0.2	0.228 ± 0.008	23.653 ± 0.031
g471	2.4	0.2	0.2	0.322 ± 0.019	23.253 ± 0.022
g472	1.6	0.5	0.5	0.400 ± 0.014	24.593 ± 0.039
g473	1.3	0.5	0.5	0.383 ± 0.012	25.057 ± 0.039
g474	1.6	0.2	0.2	0.346 ± 0.011	23.681 ± 0.041
g475	1.3	0.2	0.2	0.347 ± 0.018	24.147 ± 0.026
g476	1.6	0.1	0.1	0.293 ± 0.011	23.169 ± 0.018
g477	1.3	0.1	0.1	0.295 ± 0.016	23.616 ± 0.017
g483	0.58	0.5	0.5	0.356 ± 0.011	24.082 ± 0.039
g484	2.4	0.5	0.5	0.409 ± 0.012	24.778 ± 0.049
g485	2.4	0.1	0.1	0.328 ± 0.024	23.330 ± 0.035
g487[c]	2.4	0.5	0.5	0.349 ± 0.014	24.039 ± 0.032
g489[c]	0.35	0.5	0.5	0.320 ± 0.018	24.157 ± 0.026
g490[c]	0.58	0.5	0.5	0.375 ± 0.008	24.652 ± 0.046

[a]Where indicated, the number in the Roughness column indicates r_{min}, all other values are 0.4. The wall roughness, the friction between particles, and the friction between the particles and the walls are indicated. In all cases, shear velocity, $V_x = 1 \times 10^{-3}$ except where denoted

[b]$V_x = 1 \times 10^{-4}$.

[c]$V_x = 5 \times 10^{-4}$.

[d]Denotes $\gamma = 12$.

which increases the packing, and thus decreases overall roughness. We report wall roughness as the root mean squared roughness, R_{RMS}, which is the standard deviation of the height of the wall boundary, i.e.,

$$R_{\mathrm{RMS}} = \sqrt{\frac{1}{N}\sum_{i=0}^{N}\left(h_i - \bar{h}\right)^2} \tag{2}$$

where N is the number of samples, h_i is the measured height along the surface at a spacing of 0.05 model units, and $\bar{h}$ is the mean height of the boundary.

[21] Given in units of maximum grain radius, $R_{\mathrm{RMS}} = 2.4$ for anomalously rough boundaries, with large-amplitude grooves eight model units high, equal to those used in laboratory experiments [e.g., *Fulton and Rathbun*, 2011]. Decreasing the groove height by a factor of 2 or 4 reduces R_{RMS} to 1.6 and 1.3, respectively. Simulations without large amplitude grooves have an $R_{\mathrm{RMS}} = 0.13$, 0.35, and 0.58, which is adjusted by changing the particle size distribution in the walls. The range of R_{RMS} from 0.13 to 2.4 model units explores the range of a rough shear zone to smooth on the particle scale. A full analysis of the simulations is presented at $R_{\mathrm{RMS}} = 0.58$ and 2.4; complete roughness conditions are shown in Table 1.

[22] While DEM models in both 2-D and 3-D [*Morgan*, 1999; *Abe and Mair*, 2009] and laboratory experiments in multiple dimensions [*Knuth and Marone*, 2007] have shown that the angularity of grains is important on shear zone behavior, we choose to only use spherical grains and not bond grains together. In this configuration, DEM does capture laboratory behavior [e.g., *Knuth and Marone*, 2007 *Abe and Mair*, 2009]. This simplification allows us to run large numbers of simulations with a large number of particles, while still exploring the question of how rough shear zones interact with granular gouge particles. Models on spherical particles also allow for the comparison of our models to the large number of laboratory experiments on spherical glass beads, and for the calculation of force distribution, porosity, force fabric, and other parameters all of which are difficult with complex particles.

2.3. Scaling

[23] The model can be scaled using the grain size distribution. Because the distribution is based on a modified power law, the scaling factor is $1/r_{\max}$ of the gouge. If the largest grain of 1.0 model unit is taken to be 100 μm, a standard size for laboratory experiments, each model length unit is then 0.1 mm giving a shear apparatus of 6 mm × 3 mm × 1.8 mm. For the main suite of rough fault models, $R_{\mathrm{RMS}} = 2.4$, the grooves have amplitude of eight model units and wavelength of 10 model units, equivalent to 0.8 mm in height at a spacing of 1 mm. Throughout the paper, length units are given as the maximum grain radius, $r_{\max}$. Either the externally applied normal force F_y, or particle-particle contact force, $\boldsymbol{f}$, can be cast into dimensional quantities using Young's modulus, E, of a grain and the nominal contact area of the experiment. F_y is equal to 0.54 model unit and taking $E = 30$ GPa, normal stress in the numerical models is 15 MPa, similar to laboratory experiments on spherical glass beads.

2.4. Stress History Conditions and Strain Measurements in the Numerical Experiments

[24] Normal force, F_y, is held constant and applied equally to the solid walls on the top and bottom in all simulations (Figure 1) throughout the duration of the experiment. Both walls are allowed to move freely in the y direction to maintain F_y. After $t = 150$ model units, a constant shear velocity, V_x, is applied to the top solid wall in the x direction while bottom wall is fixed in the x dimension. This application of the displacement condition on the top block only may break the vertical symmetry of the numerical shear apparatus, explaining why, sometimes, shear localization will occur closer to the upper block and not in the center of the model.

[25] Shear velocity is then increased over $t = 450$ (Figure 2, inset) to prevent the propagation of the instability from rapidly accelerating grains. The duration of the ramp influences the initial rapidly increasing μ_{macro} portion of the friction curve but has no effect beyond a shear strain, γ, of 0.2. After $t = 600$, velocity is held steady for the duration of the experiment. Shear strain is calculated by normalizing the incremental displacement, x, by the instantaneous layer thickness, H, at each time, k over the duration of the experiment, i.e.,

$$\gamma = \sum_{k=1}^{X_{\mathrm{total}}} \frac{x_k - x_{k-1}}{H_k} \tag{3}$$

[26] To decrease the total time of each simulation, we rapidly increase shear velocity and only consider the steady state portion of the simulation. The macroscopic frictional strength, $\langle\mu_{\mathrm{macro}}\rangle$, is calculated by taking the mean of the coefficient of sliding friction at $\gamma \geq 0.4$ (Figure 2a). This range represents the steady state portion of the friction-strain curve for all tests and is beyond the evolution of layer thickness and friction resulting from initial model compaction and application of shear displacement. Small variations in μ_{macro} (Figure 2a) are caused by grain rearrangement and stick-slip; this variation is reported by taking the standard deviation about the mean of $\langle\mu_{\mathrm{macro}}\rangle$.

2.5. Calibration of the DEM Method on Experimental Data

[27] For model calibration purposes and comparison to other work, we base our simulations and scaling on the biaxial direct-shear apparatus in the Penn State Rock and Sediment Mechanics Laboratory [e.g., *Anthony and Marone*, 2005; *Rathbun et al.*, 2008; *Fulton and Rathbun*, 2011]. Experiments on this apparatus have been used for comparison to DEM models of gouge fragmentation [*Abe and Mair*, 2009], dimensionality of shear [*Knuth and Marone*, 2007], and stick-slip [*Griffa et al.*, 2011].

[28] Figure 2b presents laboratory data from an equivalent system. *Fulton and Rathbun* [2011] conducted experiments on 2 mm thick layers of soda-lime glass beads with the grain radius ranging from 50 to 80 μm, equivalent to our scaled grain size, and obtained steady state friction of ~0.4 for normal stresses in a regime where grains do not fracture. Other studies on spherical glass beads [e.g., *Mair et al.*, 2002; *Frye and Marone*, 2002; *Anthony and Marone*, 2005] also present steady state friction values ($\mu \sim 0.44$–0.47) equal to our simulations. In these laboratory experiments grains did not

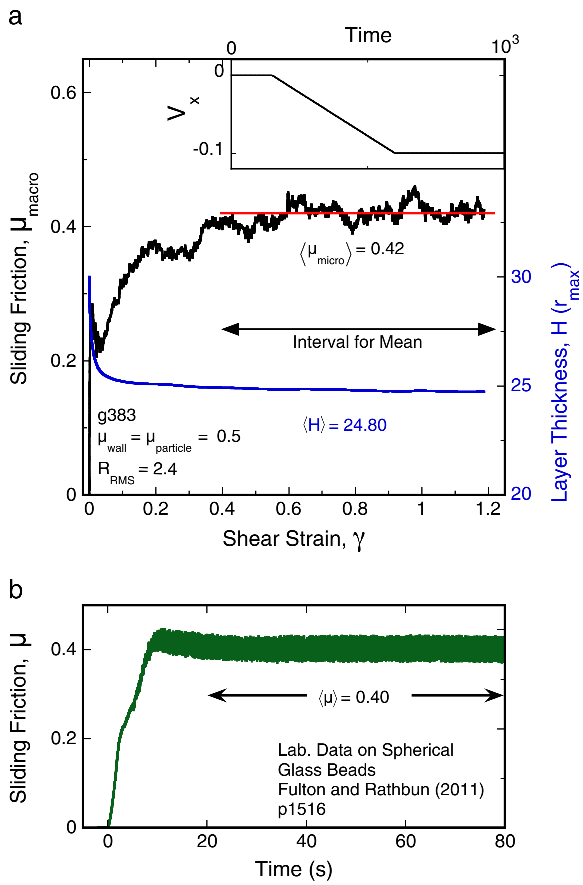

Figure 2. (a) Friction and layer thickness as a function of shear strain for the numeric experiment g382. Mean and standard deviation of μ_{macro} and H are calculated from γ 0.4 corresponding to ~700,000 numerical time steps, or $t = 21{,}000$. Units for layer thickness are given as maximum grain radius. Velocity-time history for top wall during the first 10th of the experiment, velocity, V_x, is held constant at -0.1 model unit until the completion of the experiment. (inset) The model is first compressed for $t = 150$ then velocity is ramped over $t = 450$ to avoid numeric instability. (b) Laboratory friction experiment conducted on spherical soda-lime glass beads in the same shear geometry and range in grain-size as numeric models. Laboratory experimental data from *Fulton and Rathbun*, [2011].

fracture nor become angular. The variations of $\mu_{sliding}$ displayed in Figure 2b are due to stick-slip of the granular layer in laboratory experiments. To isolate the role of particle-particle friction and wall geometry, we do not try to recreate the stick-slip phenomenon, but instead concentrate on steady-sliding in which we can investigate steady state parameters of layer thickness, friction, contact fabric and force, and other parameters that control the strength of shear zones.

3. Results

3.1. Fault Zone Strength

[29] We find that shear zone strength is a function of wall geometry and friction at particle-particle contacts and particle-wall contacts (Figure 3). For both $R_{RMS} = 0.58$ and 2.4, we analyze particle-particle friction ($\mu_{particle}$) from 0.01 to 1.0 for three different wall friction conditions, $\mu_{wall} = \mu_{particle}$, $\mu_{wall} = 0.1$, and $\mu_{wall} = 0.5$ representing a gouge zone derived from the wall rock, wall composed of weak materials, and a wall composed of strong frictional materials, respectively.

[30] For $R_{RMS} = 2.4$ (circles in Figure 3), shear zone strength, $\langle\mu_{macro}\rangle$, increases with $\mu_{particle}$ with less sensitivity to $\mu_{particle}$ at high values. The contrast between wall and gouge μ has no effect on the overall strength with all values of wall friction following the same increasing trend of $\langle\mu_{macro}\rangle$ increasing with $\mu_{particle}$. When the saw-tooth boundary is removed and the shear zone is only rough at the particle scale ($R_{RMS} = 0.58$), both $\mu_{particle}$ and the contrast between gouge and wall friction control $\langle\mu_{macro}\rangle$. The smoother shear zone boundary decreases fault strength at all μ_{wall} conditions. The contrast of μ_{wall} and $\mu_{particle}$ also influences fault zone strength for $R_{RMS} = 0.58$ boundaries. We find that when $\mu_{wall} > \mu_{particle}$ overall strength is higher. Additionally, for $\mu_{wall} = 0.1$ and $\mu_{particle} > 0.3$ frictional strength of the shear zone decreases slightly with increasing $\mu_{particle}$. We hypothesize that the difference between shear zone strength of $R_{RMS} = 0.58$ and 2.4 boundaries and the sensitivity of strength on $\mu_{particle}$ in $R_{RMS} = 0.58$ faults is due to differences in coupling between the wall and gouge zone (i.e., shear at the gouge-wall boundary), localization, and the number of grains contributing to shear. We will explore these ideas in the following sections.

3.2. Distribution of Shear

[31] To assess the cause of the variations in shear zone strength in various model conditions, we explore the degree of shear distribution in each experiment via macroscopic

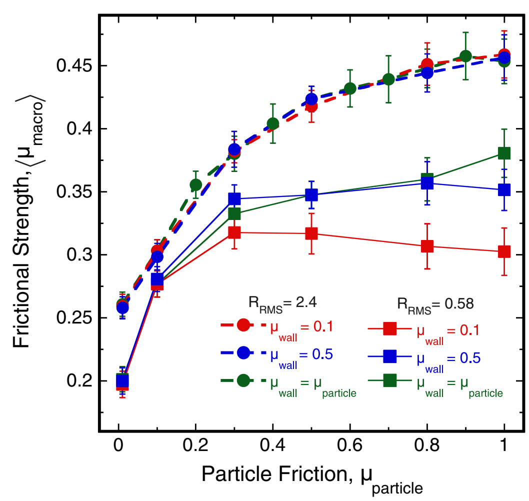

Figure 3. Steady state coefficient of sliding friction $\langle\mu_{macro}\rangle$ as a function of particle-particle and particle-wall friction, $\mu_{particle}$ and μ_{wall}, respectively. Each point represents the mean of steady state friction (i.e., Figure 2a) and uncertainty is given as one standard deviation about the mean. Circles and dashed lines correspond to rough models whereas squares and continuous lines to smooth models. Colors represent the friction of the wall-particle contact.

shear zone thickness, displacement and porosity profiles across the shearing layer, and the number of particles sliding and locked. Because each simulation starts with an equal number of particles and shear zone thickness, direct comparisons of steady state shearing thickness can be made. We take the shear zone thickness, H, as the average value of the groove-gouge interface in the simulations with grooved boundaries and as the difference between the boundaries in simulations without the grooves boundary (Figure 1).

[32] We find that $\langle H \rangle$ increases with μ_{particle} (Figure 4a). As with $\langle \mu_{\text{macro}} \rangle$, removing the large amplitude roughness decreasing R_{RMS} from 2.4 to 0.58 decreases $\langle H \rangle$. Large values of μ_{particle} show a systematic decrease in $\langle H \rangle$ when $\mu_{\text{wall}} = 0.1$. When $\langle \mu_{\text{macro}} \rangle$ is plotted as a function of $\langle H \rangle$, a clear trend emerges (Figure 4b). All R_{RMS} of 2.4 models show a linear increase of $\langle \mu_{\text{macro}} \rangle$ with $\langle H \rangle$.

[33] The same data are presented in terms of coordination number, Z_c, the number of contacts for each particle in the model in Figures 4c and 4d. Typically coordination number is denoted Z; however, we use Z_c to avoid confusion with the z-dimension. We present both $\langle H \rangle$ and $\langle Z_c \rangle$ so that the simulations can be compared with both laboratory experiments where it is impossible to observe Z_c and other simulations, which typically only present Z_c. The value of $\langle Z_c \rangle$ is calculated starting a few grain diameters from the wall to avoid influence of particles near the boundary contacting the walls. Coordination number decreases from ~5.3 at low μ_{particle} and compacted models to ~4.1 at high μ_{particle} and dilated models. Care should be taken in comparing models with and without grooves due the number of particles contacting the wall, the particles between the grooves, and frictional contrasts across the shearing zone. The contrasts across the shearing zone are displayed in Figures 5.

[34] We assess the distribution of shear by constructing a displacement profile across the layer (Figure 5). We take the difference in the x component of position, from the final to initial time, $\Delta x = (x_{\text{total}} - x_i)$, against the final y position of the particle in the layer, y_f. To calculate the profile, we bin y_f into 100 equal bins and average along the z dimension.

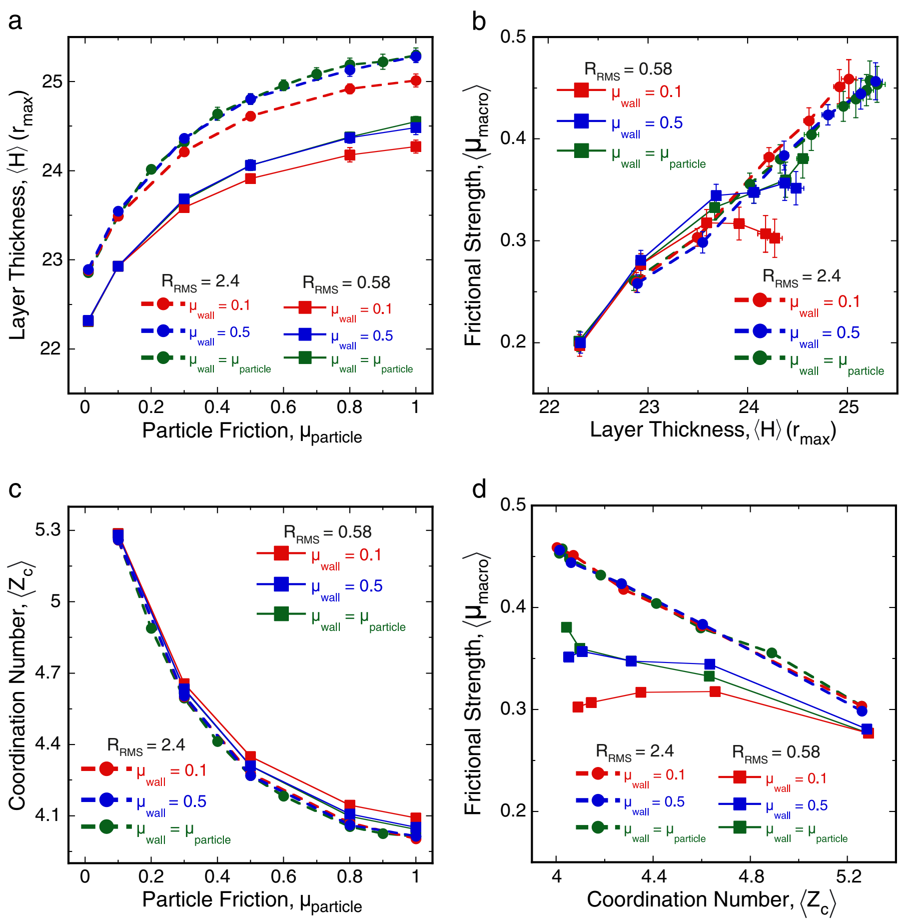

Figure 4. (a) Steady state thickness of the gouge layer, $\langle H \rangle$, as a function of particle-particle friction, μ_{particle}. (b) Frictional strength plotted as a function of layer thickness, values of strength correspond to the points in Figure 3. (c) Mean coordination number, $\langle Z_c \rangle$ as a function of μ_{particle}. (d) Frictional strength as a function of $\langle Z_c \rangle$. Mean values are taken from the steady state portion of the friction and layer thickness trend (Figure 2). Uncertainty in $\langle H \rangle$ and $\langle Z_c \rangle$ may be smaller than the diameter of the data symbols. Circles and dashed lines correspond to rough models whereas squares and plain lines to smooth models. Colors represent the friction of the wall-particle contact. Units for layer thickness are given as maximum grain radius.

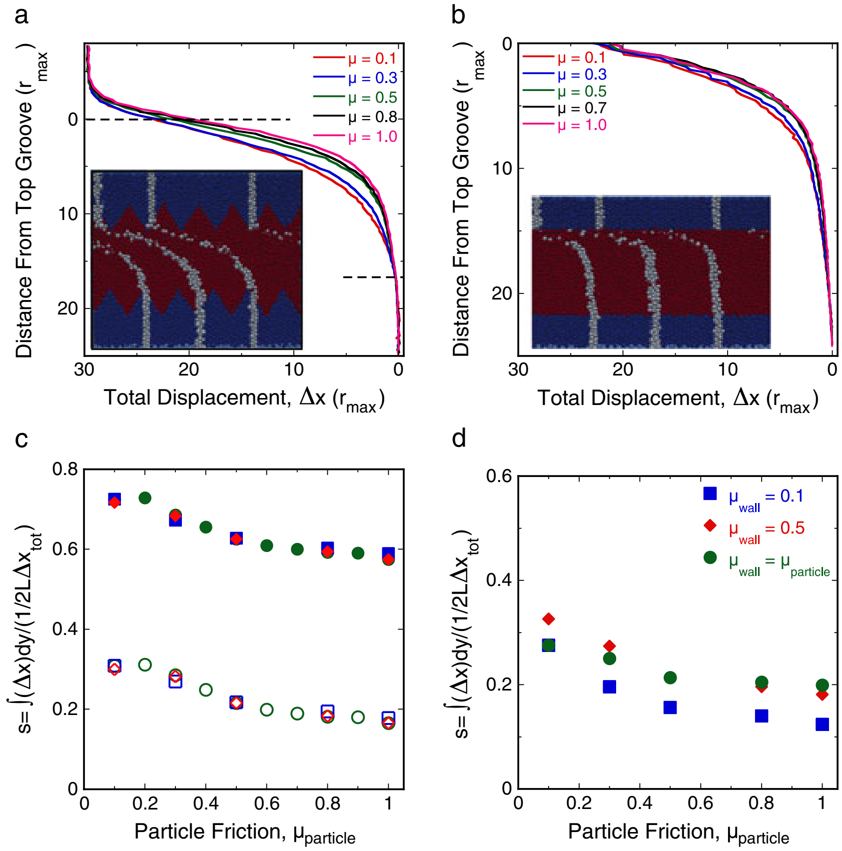

Figure 5. Displacement in the shear (x) direction as a function of position in the layer (y position) for (a) $R_{\mathrm{RMS}} = 2.4$ and (b) $R_{\mathrm{RMS}} = 0.58$. Gouge particle positions are binned in the y dimension and averaged in each bin. Traces correspond to $\mu_{\mathrm{wall}} = \mu_{\mathrm{particle}}$ (green circles in Figure 3). Dashed lines represent the groove tip in $R_{\mathrm{RMS}} = 2.4$. Image of the final time of the simulation, strain markers (grey) are included by coloring some particles and were initially vertical (inset). In all simulations, the bottom wall remained fixed and the top was displaced $\Delta x = 30$. Area under the curve in the y-direction normalized by a profile assuming purely distributed shear. (c) $R_{\mathrm{RMS}} = 2.4$ with closed symbols representing the total thickness of all gouge particles and open symbols the area between the dashed lines (groove tips). (d) $R_{\mathrm{RMS}} = 0.58$. Units for distance are given as maximum grain radius.

[35] All experiments are sheared to total displacement $\Delta x_{\mathrm{total}} = 30$ model units. For rough shear zones, grains nearest to the top wall shear 30 units; however, Δx begins to decrease within the grooves (groove tips are denoted by black, dashed lines in Figure 5a) and progressively decreases to zero at the bottom of the model (Figure 5a). Experiments in the absence of grooves show offset at the particle-wall boundary (Figure 5b), indicating a partition of slip between shearing of the gouge layer and slip at the interface due to low coupling. The displacement profiles show a clear trend of decreasing displacement into the layer with μ_{particle}. There is a contrast in the degree of shear distribution from low to high friction.

[36] We quantify each shear profile by taking the integral in the y direction and comparing the integral to the triangle that defines the possible displacement, i.e.,

$$s = \frac{\int_{y\,\mathrm{min}}^{y\,\mathrm{max}} \Delta x dy}{1/2 H_{\mathrm{eff}} \Delta x_{\mathrm{total}}} \tag{4}$$

where $\Delta x_{\mathrm{total}}$ is the total displacement (30 model units in most experiments), H_{eff} is the thickness of the layer contributing to shear, i.e., the difference between the maximum point of the layer, y_{max}, and minimum point, y_{min}. In this relation, when $s = 0$ there is no shear in the layer and all displacement is at the gouge-wall interface, $s = 1$ when shear progressively decreases from 30 at the top of the layer to 0 at the bottom, and $s = 2$ if the entire layer moves by offsetting at the bottom.

[37] To account for the difference between a shear zone with grooves and without grooves (i.e., Figures 1a versus 1b), we calculate s in grooved wall models using two end-member situations: (1) the total height of the granular shear zone, including particles trapped between large-scale roughness at the top and bottom of the shear zone as closed symbols in Figure 5c and (2) the zone between the groove tips (dashed lines) as open symbols in Figure 5c. For both $R_{\mathrm{RMS}} = 0.58$ and 2.4 boundaries, the quantity of s is less than 1, indicating decreased shear away from the moving upper wall. In both cases, s decreases with μ_{particle} indicating more localization of shear near the upper boundary with high μ_{particle}. For $R_{\mathrm{RMS}} = 0.58$, μ_{wall} and μ_{particle} contribute to the

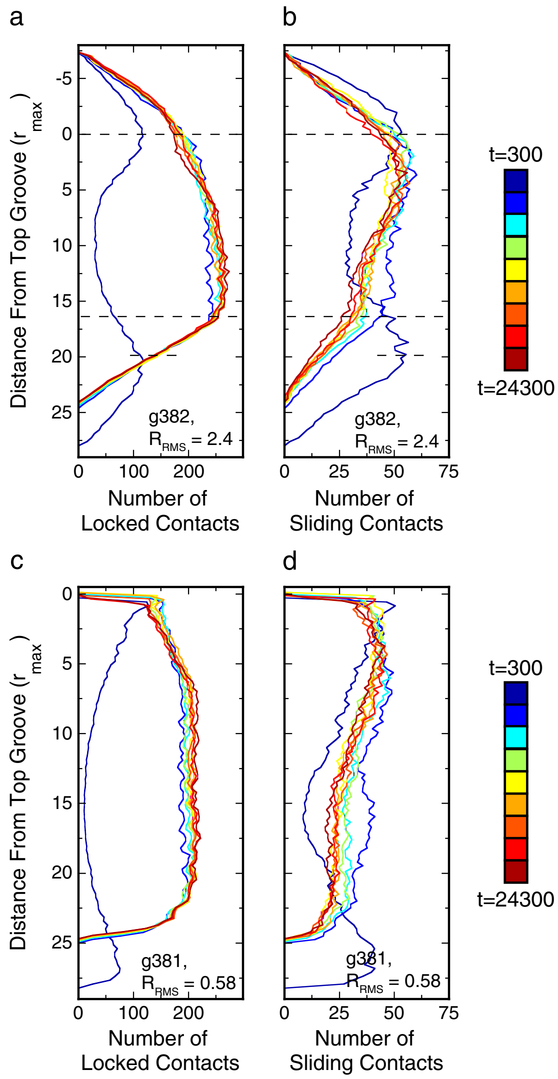

Figure 6. The number of (a and c) locked and (b and d) sliding contacts as a function of position across the model for $\mu_{wall} = \mu_{particle}$. Data are binned in the y dimension and averaged in each bin. Each trend represents a different time in the model with time given in the color bar. $R_{RMS} = 2.4$ (Figures 6a and 6b), dashed lines represent the tip position of the grooves. $R_{RMS} = 0.58$ (Figures 6c and 6d). Units for distance are given as maximum grain radius.

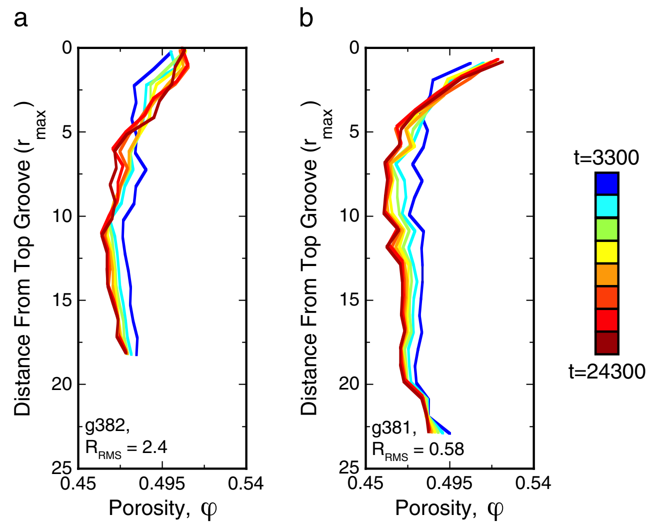

Figure 7. Porosity profiles across the shearing layer for (a) $R_{RMS} = 2.4$ and (b) $R_{RMS} = 0.58$. Color represents time and is given in the legend. In $R_{RMS} = 2.4$ models, the porosity is only calculated between the groove tips. Units for distance are given as maximum grain radius.

profile of shear (Figure 5d). Low μ_{wall} induces less shear in the layer because it is more efficient to displace at the wall-particle boundary. For $R_{RMS} = 2.4$, the geometry and $\mu_{particle}$ control local Δx, with all μ_{wall} values producing the same s. In all cases, high $\mu_{particle}$ enhances localization near the top boundary.

[38] To further assess the distribution of shear, we present the number of sliding and locked contacts as a function of height across the layer. Figure 6 presents representative simulations for $R_{RMS} = 2.4$ (Figures 6a and 6b) and $R_{RMS} = 0.58$ (Figures 6c and 6d) boundaries, both at $\mu_{wall} = \mu_{particle} = 0.5$. As with the shear profiles, the data are binned in the y dimension and the number of contacts that are sliding and locked are counted at intervals of 3000 time steps beginning at $t = 300$ (Figure 6). Sliding contacts are defined as any particle that overcomes its Coulomb criterion, irrespective if that failure is via sliding or rolling. Starting at $t = 300$ allows investigation of the layer before the initiation of shear, but after the application of normal force. Because the layer is compressing in the normal direction, the trend contains two humps near the boundaries. Once displacement of the walls begins, this trend disappears and many more grains are in contact. For both $R_{RMS} = 2.4$ (Figure 6a) and $R_{RMS} = 0.58$ models (Figure 6c), the number of locked contacts increases with distance from the top, shearing wall. The number of locked contacts increases to ~7.5 model units from the top groove in models with grooves or top wall in models absent of high amplitude roughness. Beyond a distance of 7.5 model units the number of locked contacts stays approximately constant with depth. A slight evolution is present with time with the number of locked contacts increasing with time from $t = 3300$ to $t = 27{,}300$. This temporal difference is more apparent in the sliding contacts (Figures 6b and 6d). At $t = 3300$ more contacts are sliding over the entire thickness than at $t = 27{,}300$ with a progressive decrease in time. The absolute number of sliding and rolling contacts decreases with depth from the top lowest extent of the wall after the first ~7.5 model units

[39] The evolution of sliding and locked contacts, both in time and space helps to explain the displacement profiles presented in Figure 5. The amount of Δx rapidly decreases with depth in the model until ~7.5 model units and is then near zero. This is reflected by the increasing number of locked contacts to this depth and decreasing number of sliding contacts. Additionally, the temporal transition of locked and sliding contacts corroborates shutting down of shear in the lower portion of the shear zone and more localization of shear near the top boundary. Note also that this asymmetry comes from the loading condition and sliding style. Shear velocity is imposed on only the top

block, breaking the vertical symmetry of the system. In thin shear zones relative to the groove height and particle radius, shear would be distributed over the entire thickness because the decay of Δx as a function of distance from the shearing wall cannot be manifested. In these simulations, the shear zone is tens of particles thick allowing shear to localize. Calibration models in which both walls were sheared contain vertical symmetry.

[40] Initial porosity, $\phi = 0.56$, is high due to the narrow grain size distribution. As evidenced by the decrease in layer thickness from $t = 0$ (Figure 2), ϕ initially decreases in time as normal stress is applied. As with the trends of $\langle \mu_{macro} \rangle$, $\langle H \rangle$, and the number of sliding and locked contacts, ϕ becomes steady with time or strain shortly into the model (Figure 7). As with both the number of sliding and locked contacts, porosity is plotted at multiple times to show the natural variation in the system. Because the number of shearing particles varies as a function of y position, ϕ varies as a function of height across the layer facilitating dilation across the layer and the need for particles to rearrange (Figure 7). Porosity decreases by ~0.04 in the first 7.5 units from the top groove (or wall in $R_{RMS} = 0.58$ simulations). Beyond 7.5 model units, ϕ stays near constant across the layer.

3.3. Particle-Particle Force

[41] Microscopic force parameters are quantified by investigating the magnitude of the force between two particles, orientation of the contacting grains, and the orientation of the force between the grains. Force fabric and magnitude statistics are analyzed for all frictional (gouge) particles in the model through one simulation and by comparing mean values of one simulation to another.

[42] To investigate the force chain fabric, two populations of contact forces are considered, grain-grain contacts above the mean force of all contacts ($\boldsymbol{f}/\|\boldsymbol{f}\| > 1$) termed "strong contacts" and "weak contacts" below the mean force ($\boldsymbol{f}/\|\boldsymbol{f}\| \leq 1$) [*Radjaï et al.*, 1996; 1998]. Strong contacts have been hypothesized to be part of force chain networks, a long-lived collection of contacting grains that can branch across the layer, while the weak contacts act to buffer and support the chains [*Radjaï et al.*, 1996, 1998; *Aharonov and Sparks*, 2004; *Mair and Hazzard*, 2007].

3.3.1. Force Magnitude

[43] The magnitudes of particle forces, $\boldsymbol{f}$, are quantified for the overall average force and the distribution of the force magnitude. The mean force, $\|\boldsymbol{f}\|$, is calculated by averaging the norm of force vector between contacting particles for each contact in the simulation. The distribution of the force magnitudes follows a probability density function (PDF) that is well fit by an exponential (Figure 8a)

$$P(f) \propto e^{-\beta \frac{f}{\|f\|}} \tag{5}$$

where $\boldsymbol{f}$ is normalized by $\|\boldsymbol{f}\|$ [*Liu et al.*, 1995]. We calculate $P(\boldsymbol{f})$ using (5) at 100 times in the model for forces $1 < \boldsymbol{f}/\|\boldsymbol{f}\| \leq 7$. The fit range represents values over the mean, which is expected to be in force chains and ignores any anomalously large forces, which may be present on one grain, i.e., Figure 8a.

[44] From $\boldsymbol{f}/\|\boldsymbol{f}\|$ of 1 to 7, an exponential decrease in force is observed and described by the slope β. For the weak

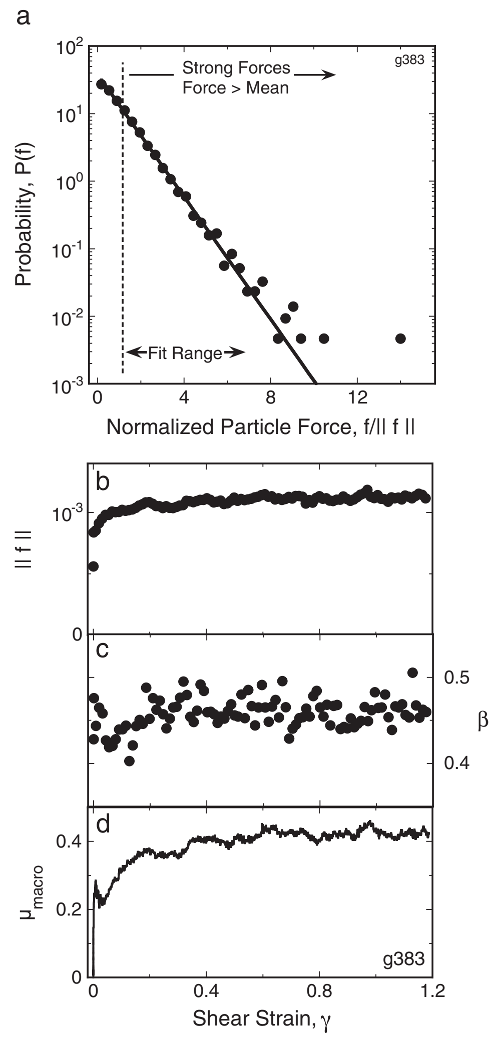

Figure 8. Interparticle force magnitude statistics for one numerical experiment (g383, see Table 1) as a function of strain, γ. (a) Calculation of the probability density function (PDF) of particle force at $\gamma = 0.6$. Data are fit over $1 < \boldsymbol{f}/\|\boldsymbol{f}\| \leq 7$, the mean force to seven times the mean force using equation (5). (b) Mean particle force at 100 equally spaced times in experiment g383. (c) Slope of the PDF calculated in Figure 8a and given as a function of γ. (d) Friction-strain curve for experiment g383.

contact network ($\boldsymbol{f}/\|\boldsymbol{f}\| \leq 1$), the exponential relation (5) no longer holds. The value of $\|\boldsymbol{f}\|$ rapidly increases to near steady at small γ (Figure 8b). Variations in the macroscopic parameter μ_{macro} are reflected in $\|\boldsymbol{f}\|$, albeit as small fluctuations. As with $\|\boldsymbol{f}\|$, β reaches a steady value at low γ. While the variations of μ_{macro} are not reflected in $\|\boldsymbol{f}\|$, large variations in β are observed (Figure 8c).

[45] To compare experiment-to-experiment variation, $\langle f \rangle$ is defined as the mean of $\|\boldsymbol{f}\|$ for all particle-particle contacts at $\gamma > 0.4$. Experiments with $R_{RMS} = 2.4$ have a larger value of $\langle f \rangle$ than experiments with $R_{RMS} = 0.58$ (Figure 9a). We find that $\langle f \rangle$ increases with $\mu_{particle}$ in all cases. Wall friction has little to no influence on $\langle f \rangle$ when $R_{RMS} = 2.4$, while there is a systematic variation $R_{RMS} = 0.58$. The constant value of $\langle f \rangle$ for $R_{RMS} = 2.4$ at various μ_{wall} indicates that the normal (elastic) force is the dominant intergranular force, not the

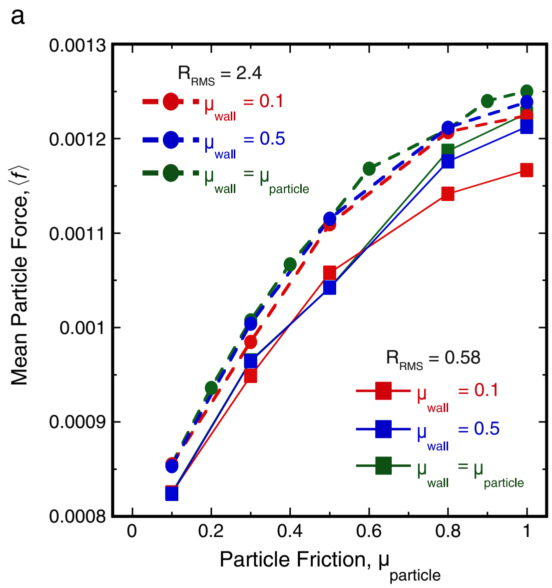

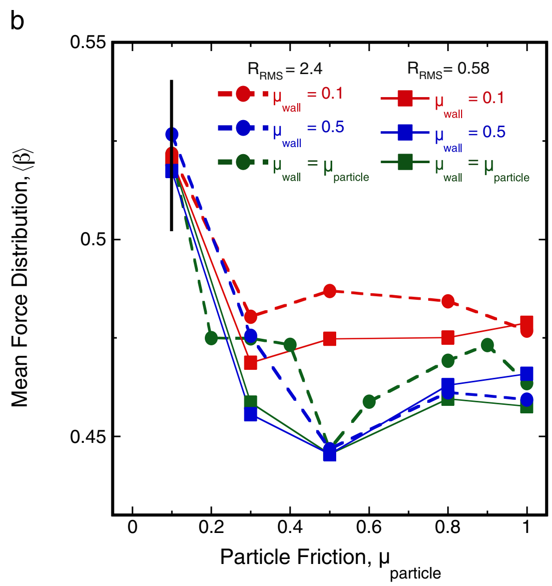

Figure 9. (a) Mean particle force $\langle f \rangle$ for each particle friction and wall condition. Error bars are smaller than symbol size. (b) Mean force magnitude distribution, $\langle \beta \rangle$. Means are taken at $\gamma > 0.4$ (Figure 8d). A representative error bar is given in black at $\mu_{particle} = 0.1$. Circles and dashed lines correspond to rough models whereas squares and continuous lines to smooth models. Colors represent the friction of the wall-particle contact.

shear component of intergranular force. The variation in β and the large standard deviation make analyzing the distribution of forces from the probability density function (Figure 9b) difficult; however, some systematic trends do emerge. The force distribution is constant with $\mu_{particle}$ above 0.3 when considering the uncertainty in β (Figure 9b). Also, rough walls tend to promote a large $\langle \beta \rangle$ and $\langle f \rangle$ at each friction condition indicating that more of the overall force is contained in the high force network. This indicates that mean force in the model is large; however, a smaller proportion of grains have large forces acting on them and the high force network is supported by fewer contacts.

3.3.2. Contact Fabric and Force Orientation

[46] Particle contact orientation is quantified using a polar histogram of each contact and fitting a function around the histogram using the method of *Rothenburg and Bathurst* [1989]. The orientation vector between the center of mass of two contacting particles (e.g., Figure 10) is written in polar terms in the *x-y* and *x-z* directions. The angular distribution of contacts, $E(\theta)$, is described by using the second Fourier component of $E(\theta)$, i.e.,

$$E(\theta) = \frac{1}{2\pi}\{1 + a\cos 2(\theta - \theta_a)\} \tag{6}$$

where a defines the magnitude of anisotropy, and θ_a is the direction of anisotropy. A complete explanation of the method can be found in *Rothenburg and Bathurst* [1989].

[47] As with the analysis of β, we threshold above and below $\boldsymbol{f}/\|\boldsymbol{f}\| = 1$ and report a and θ as a_w, θ_w and a_s, θ_s for weak and strong contacts, respectively.

[48] Figure 11 displays the calculation of a_w, θ_w, a_s, and θ_s. The polar histogram represents all contacts at the mid-time of experiment g383 with the fit of equation (6) for each family of contacts in the *x-y* and *x-z* directions. Weak contacts are near isotropic in the *x-y* direction with $a_w = 0.058$ and $\theta_w = 47.6°$ while strong contacts are anisotropic in the *x-y* direction with $a_s = 0.49$ and $\theta_s = 50.1°$. When $a = 0$, the fabric is isotropic with equation (4) producing a circle and thus the value of θ_w has little meaning. Weak contacts are isotropic in the *x-z* direction in all cases (Figure 11b). Strong contacts preferentially align into the shear direction. Beyond a few degrees from the shear direction in *x-z* space, contacts are isotropic.

[49] Contact fabric is quantified at 100 temporally equal spacing for each experiment in the *x-y* direction. As shear initiates and friction rises, θ_s rotates from the normal direction at ~90° to a steady value at ~50° (Figure 12a). The rotation of contact orientation is accompanied by an increase in a_s from ~0.3 to ~0.48 (Figure 12b). Weak contact fabric increases in anisotropy from near 0 to between 0.05 and 0.1 and retains a large number of contacts in all directions (Figure 12d).

[50] Mean values of contact fabric are computed at $\gamma > 0.4$ for each simulation (Figure 13). For strong contacts, $\langle a_s \rangle$ is larger in simulations with $R_{RMS} = 2.4$ boundaries. In $R_{RMS} = 0.58$ models, the value of μ_{wall} influences anisotropy. The value of $\mu_{particle}$ has little overall effect on $\langle a_s \rangle$ (Figure 13a).

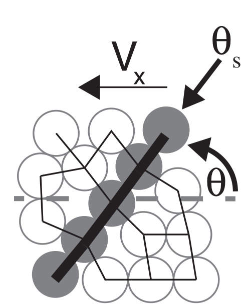

Figure 10. Two-dimensional example of the contact network. Solid circles and bold lines represent strong force contacts that are aligned in the θ_s direction. Sense of shear is top to the left.

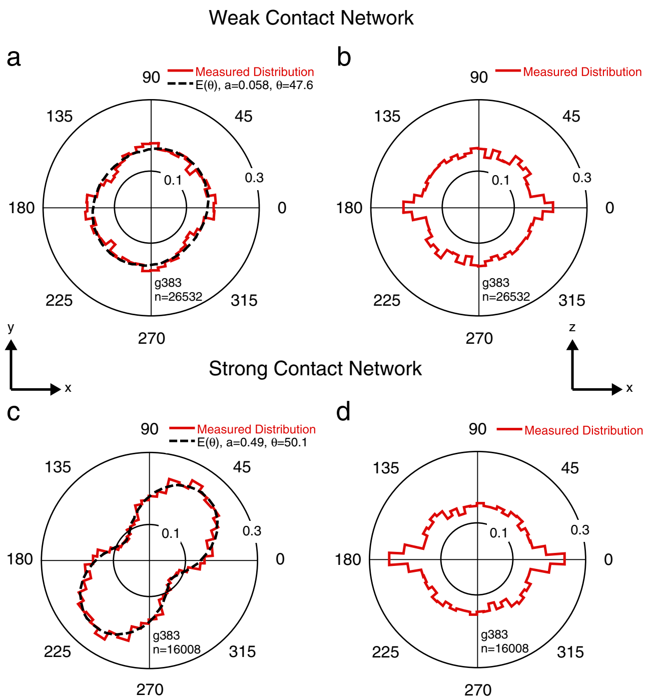

Figure 11. Calculation of contacts' orientations. The proportion of particle contact orientation is binned (solid line) and fit (dashed line) using equation (6). Best fit parameters are given in the legend. The number of contacts is given as n. The radius represents the proportion of contacts for weak contacts, $\boldsymbol{f}/\|\boldsymbol{f}\| \leq 1$ and strong contacts, $\boldsymbol{f}/\|\boldsymbol{f}\| > 1$. Sense of shear is top wall in $-x$ direction. (a) Weak contact network in the x-y direction (side view of the shear zone). (b) Weak contact network in the x-z direction (top view). (c) Strong contact network in the x-y direction (side view). (d) Strong contact network in the x-z direction (top view).

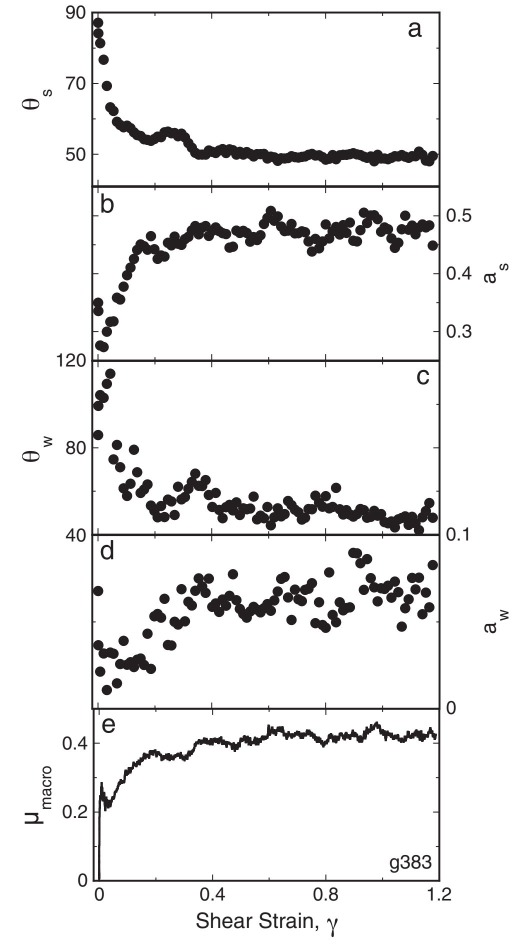

Figure 12. Interparticle force orientation for all contacts in the x-y direction during one experiment as a function of strain. (a) Orientation of strong force contacts. (b) Anisotropy of strong force orientation. (c) Orientation of weak force contacts. (d) Anisotropy of weak force contacts. (e) Friction-shear strain. The fits given in Figure 11 correspond to $\gamma = 0.5$.

Orientation of contacts is slightly more shear normal position with increased μ_{particle} (Figure 13b). Boundaries of $R_{\text{RMS}} = 0.58$ also have a more shear normal orientation by a few degrees than $R_{\text{RMS}} = 2.4$. The weak contact fabric anisotropy increases with μ_{particle}; however, the network remains nearly isotropic for all models (Figure 13c). Boundaries with $R_{\text{RMS}} = 0.58$ are systematically more isotropic than rough boundary models. The orientation, $\langle\theta_w\rangle$ displays a large difference between $R_{\text{RMS}} = 0.58$ and 2.4; however, the small value of $\langle a_w\rangle$ indicates that large numbers of weak contacts are present in all orientations. The anisotropy of contact networks for strong forces indicates that few of the high force contacts occur at angles larger or smaller than $\langle\theta_s\rangle$. This implies that the force chain network $\boldsymbol{f}/\|\boldsymbol{f}\| > 1$ exists almost exclusively in the direction of $\langle\theta_s\rangle$.

[51] Similar to contact orientation, the orientation of normal component of the interparticle force can be quantified by

$$\bar{f}_n(\theta) = \bar{f}_0\{1 + a_n \cos 2(\theta - \theta_f)\} \tag{7}$$

where $\bar{f}_n$ is the mean normal force between particles, a_n is the anisotropy of the normal force, and

$$\bar{f}_0 = \int_0^{2\pi} \bar{f}_n(\theta)d\theta \tag{8}$$

[*Rothenburg and Bathurst*, 1989]. Values and trends of $\langle a_n\rangle$ and $\langle\theta_f\rangle$ track $\langle a_s\rangle$ and $\langle\theta_s\rangle$ indicate that most of the force that supports the grain network is oriented perpendicular to grain contacts, in the grain normal direction.

3.4. The Role of Fault Zone Roughness on Strength and Force Parameters

[52] To further elucidate the role of fault zone roughness on strength and particle-particle force, additional simulations with varied R_{RMS} were analyzed. The size of the grooves is decreased from eight model units to two and four model units, or $R_{\text{RMS}} = 1.3$ and 1.6, respectively. To construct shear zones that are smooth to the particles, the range is increased between the maximum and minimum radius of the grains that construct the walls. In all cases, the $r_{\max}$ is constant at 1.0 unit and $r_{\min}$ is decreased. In the main suite of experiments comparing grooved walls and smooth walls, $r_{\min}$ is 0.4 which yielded $R_{\text{RMS}} = 2.4$ and 0.58 with and without grooves, respectively. The $r_{\min}$ is decreased to 0.25 and 0.125 increasing the packing and thus decreasing R_{RMS} to 0.35 and 0.13, respectively.

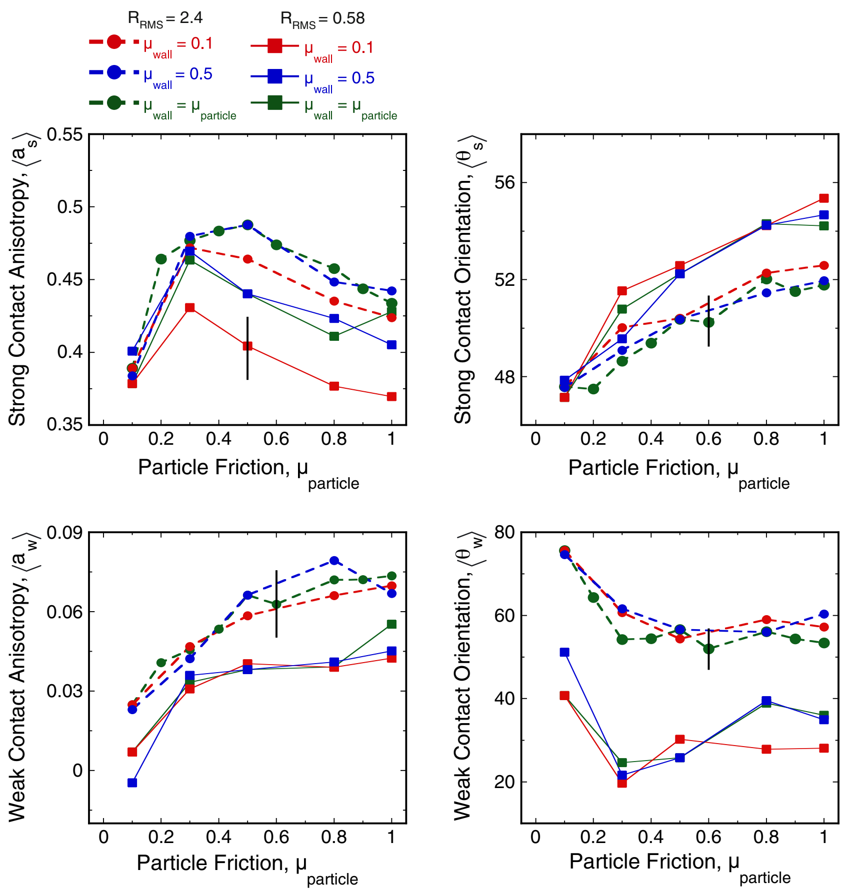

Figure 13. Orientation statistics for each model condition in the *x-y* direction. Circles and dashed lines correspond to $R_{\mathrm{RMS}}=2.4$ whereas squares and continuous lines to $R_{\mathrm{RMS}}=0.58$. Colors represent the friction of the wall-particle contact. A representative error bar is included in black in each panel. (a) Anisotropy of strong contacts. (b) Orientation of strong contacts. (c) Weak contact anisotropy. (d) Weak contact orientation.

[53] The lack of coupling between the wall and granular shear zone decreases the overall strength via offset at the wall-gouge boundary. As R_{RMS} decreases in simulations in the absence of grooves, fault zone strength decreases linearly for a given μ_{particle} (Figure 14a). Roughness controls the slope of the trend and μ_{particle} controls the intercept. Above a critical R_{RMS}, the linear trend breaks and the contribution of μ_{particle} becomes the controlling factor in strength with R_{RMS} having little to no influence. The transition corresponds to near the radius of the median particle size of the gouge (Figure 14a).

[54] Displacement profiles across the shearing zone highlight the differences caused by boundary roughness (Figure 14b). Below $R_{\mathrm{RMS}}=1$, displacement profiles are dependent on wall roughness with significant offset between the wall and gouge zone. In all cases, the wall is displaced a total of 30 model units; however the largest amount of displacement in the gouge depends on μ_{particle} and more importantly on R_{RMS}. When analyzing $\mu_{\mathrm{particle}}=0.5$, the maximum displacement in the gouge decreases from 21.2 at $R_{\mathrm{RMS}}=0.58$, the roughest boundary without grooves, to 15.0 and 11.5 at $R_{\mathrm{RMS}}=0.35$ and 0.13, respectively (Figure 14b). Cast into terms of *s*, these trends represent 0.21, 0.15, and 0.10 from roughest to smoothest. All three conditions with large boundary roughness due to the presence of a grooved wall (R_{RMS} of 1.3, 1.6, and 2.4) have no offset between the wall and gouge zone, and thus a negligible difference in shear zone strength (Figure 14a).

[55] Decreasing R_{RMS} elucidates trends in grain contact orientation and force chains. Using equation (4) to analyze the orientation of strong contacts, we show that roughness increases the anisotropy factor $\langle a_s \rangle$ (Figure 14c). Simulations without grooved boundaries ($R_{\mathrm{RMS}}<1$) produce a near linear decrease of $\langle a_s \rangle$ with R_{RMS}. Adding grooves, and roughness to the shear zone, increases $\langle a_s \rangle$ indicating that more grain contacts are orienting into a preferred direction with less branching in the force chains. The factor $\langle a_s \rangle$, becomes insensitive to R_{RMS} above 1. A slight decrease in anisotropy occurs due to the contacts between the large amplitude grooves at $R_{\mathrm{RMS}}=2.4$.

[56] Orientation of the strong contacts rotates into the shear direction with increased fault zone roughness (Figure 14d). Because strong contacts support the jammed, non-shearing network of contacts [*Radjaï et al.*, 1998; *Walsh et al.*, 2007], it is expected that a jammed network would have a high angle, closer to the direction of the normal force. In the simulation of $R_{\mathrm{RMS}}=0.13$ and $\mu_{\mathrm{particle}}=0.5$, the preferred orientation is $\langle \theta_s \rangle = 57.5°$. The angle θ_s decreases systematically as the fault zone roughens and is ~50° at $R_{\mathrm{RMS}}=2.4$.

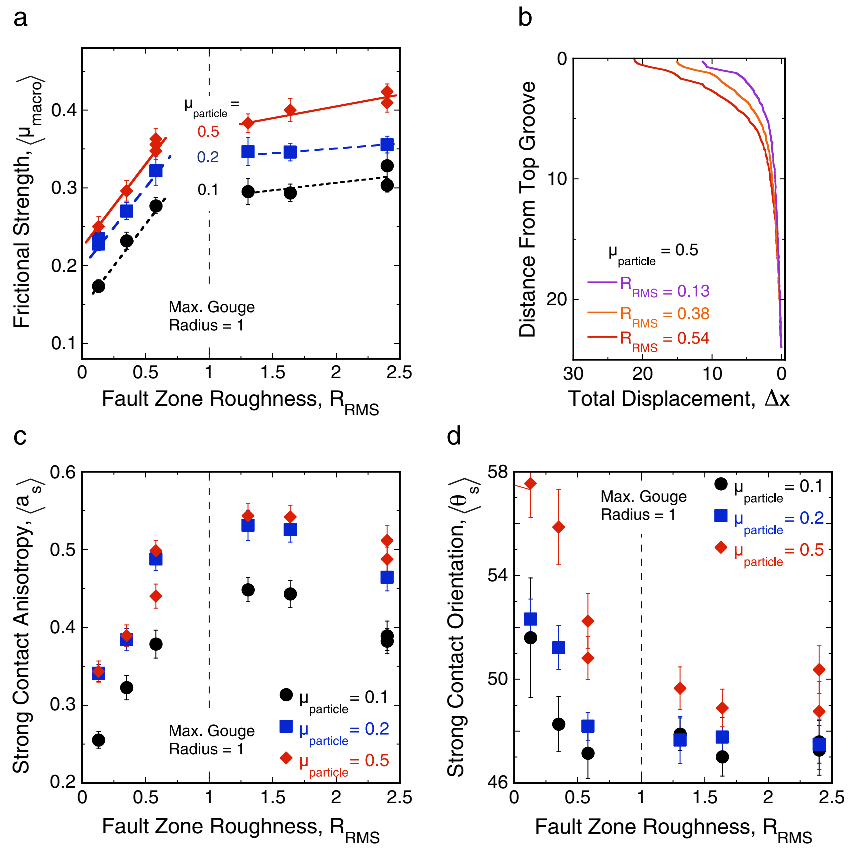

Figure 14. Role of fault zone roughness. (a) Shear strength as a function R_{RMS} for $\mu_{\mathrm{particle}} = 0.1$, 0.2, and 0.5. (b) Displacement profiles across the shearing layer for simulations without grooved boundaries and $\mu_{\mathrm{particle}} = 0.5$. (c) Contact anisotropy as a function of R_{RMS}. (d) Contact orientation as a function of R_{RMS} . Units for distance and displacement are given as maximum grain radius. In Figures 14a–14d, the vertical dashed line represents the maximum radius of a gouge particle.

4. Discussion

4.1. Roughness and Frictional Coupling

[57] The coupling of the shear zone wall and granular layer causes the differences in strength with different R_{RMS}. Coupling is controlled by two factors, albeit in different proportions. First, the dominant fault zone geometry and second, fault zone friction between the gouge-gouge and gouge-wall interactions. When a fault is anomalously rough, $R_{\mathrm{RMS}} > 1$ (the maximum grain radius) in these simulations, the wall is well coupled to the gouge and gouge properties control behavior. The large amplitude roughness necessitates that all the deformation occurs within the shearing layer and not at the gouge-wall interface with no offset between the wall and the gouge (Figure 5). Due to large roughness, any difference between the friction of the wall and gouge is largely unimportant to the overall strength because the normal (elastic) force between the wall and gouge controls behavior. When large amplitude roughness is removed and the shear zone is only rough on the grain-scale, the tangential force, wall friction, becomes a controlling factor in determining whether the fault and gouge are coupled together.

[58] *Shojaaee et al.* [2012b] simulated 2-D disks between infinitely smooth walls and vary both μ_{particle} and μ_{wall}. Their results quantitatively agree with our simulations that $\langle\mu_{\mathrm{macro}}\rangle$ becomes insensitive to μ_{particle} at values ~0.7. The wall offsets at the boundary the granular shear with values of μ_{wall} controlling the amount of offset. At extremely low μ_{wall} and an infinitely smooth wall, no shear occurs in the granular layer [*Shojaaee et al.*, 2012b]. *Shojaaee et al.* [2012b] find that, as the wall roughness increases, frictional strength of the system increases and eventually becomes independent of roughness, agreeing with our simulations (Figure 14a).

[59] Our results of roughness and asperities controlling the strength of a system agree with well-known engineering relations of roughness and friction on bare surface experiments [e.g., *Bowden and Tabor*, 1950]. Experiments on diamond coatings show that friction increases with roughness and that as wear is produced, the roughness is decreased, dropping the strength [*Hayward et al.*, 1992].

4.2. Comparison to Laboratory Strength Measurements

[60] Simulations of rough boundaries and spherical particles reproduce the strength measured in the laboratory [*Abe and Mair*, 2009]. Our simulations capture the frictional strength of spherical glass beads with rough boundaries [e.g., *Mair et al.*, 2002; *Frye and Marone*, 2002; *Anthony*

and Marone, 2005; *Fulton and Rathbun*, 2011]. Previous studies on 3-D DEM have failed to capture the behavior of laboratory experiments of spherical beads and machine polished smooth steel [i.e., *Anthony and Marone*, 2005]. Progressively decreasing the roughness of the fault (Figure 14) shows a linear decrease of strength with roughness. If the data are extrapolated to a theoretical shear zone that is infinitely smooth, simulations suggest that the strength is $\langle \mu_{macro} \rangle \approx 0.15$, equal to $\mu_{macro} \approx 0.13$ reported by *Anthony and Marone* [2005] when using $\mu_{wall} = \mu_{particle} = 0.1$ as suggested from the experimental data of *Frye and Marone* [2002].

4.3. Overall Shear Zone Strength and the Role of Shear Distribution

[61] Frictional strength, $\langle \mu_{macro} \rangle$, varies as a function of $\langle H \rangle$, or $\langle Z_c \rangle$ (Figure 4). Since the main suite of the simulations starts with the same layer thickness, number of particles, and packing of the wall, the overall thickness of the layer during shear reflects differences at the microscale in the gouge. Comparing values of $\langle H \rangle$ with local porosity (or coordination number) across the shearing layer shows that the degree of dilatancy is high close to the moving boundary and transitions to packed or jammed state far from the boundary. We find that there is a trade-off between $\langle H \rangle$ and the degree of localization, s.

[62] High $\mu_{particle}$ leads to more localization of shear near the boundary and lower s, because it is more efficient to shear a few grains rather than mobilize a large number of high $\mu_{particle}$ contacts. This leads to enhanced shear in the boundary and increased dilation. High dilation is manifested as high ϕ or low Z_c, in the zone and a larger overall $\langle H \rangle$. The value of Z_c is lower in the actively shearing portion of the layer, than in the locked contacts and the bottom of the shear zone.

[63] The DEM simulations in 2-D show that Z_c decreases with increased $\mu_{particle}$ [*Morgan and Boettcher*, 1999; *da Cruz et al.*, 2005; *Makedonska et al.*, 2011; *Shojaaee et al.*, 2012a] and simulations in 3-D yield equivalent Z_c values as our simulations [*Silbert et al.*, 2002a]. *Marone et al.*, [1990] proposed a simple work balance based on a linear relation of friction and dilation based on shear experiments with angular gouge. *Makedonska et al.* [2011] defined fields where the linear relationship of $\langle \mu_{macro} \rangle$ and $\langle H \rangle$ (or $\langle Z_c \rangle$) is expected to break due to transitions of styles of grain motion such as particle rolling. As shown in the models of *Makedonska et al.* [2011], high friction particles prefer rolling, while low friction particles move by a combination of rolling, sliding, and distribution of shear. In our simulations, we find that frictional strength is linear with coordination number over the range of all values for rough boundaries. In smooth boundary simulations, frictional strength is lower than rough boundary simulations for the same coordination number due to grains near the boundary preferentially rolling at high $\mu_{particle}$ distributing less shear into the layer (Figure 5), and promoting offset at the boundary of the gouge and wall. We do not consider the change in ϕ or Z_c with strain in these simulations and second-order friction variations. For a complete discussion of the role of changing Z_c and μ, please see *Marone et al.* [1990] and *Mair and Abe* [2008].

4.4. Displacement Profiles

[64] Shear profiles show enhanced displacement near the moving boundary. Similar profiles are observed in 2-D models of *Aharonov and Sparks* [2002] and 3D models of *Mair and Hazzard* [2007]. The models of *Mair and Abe* [2008] present similar shear profiles to our simulations, but the models are not directly comparable due to large amounts grain fracture of the gouge. Additionally, our observed profile is common in laboratory experiments of granular shear at low stress and high strain rates [e.g., *Pouliquen and Gutfraind*, 1996; *Veje et al.*, 1999; *Losert et al.*, 2000; *Mueth et al.*, 2000; *Bocquet et al.*, 2002; *Tsai and Gollub*, 2005; *van der Elst et al.*, 2012] showing what can be approximated as an exponential decay of shear velocity of displacement going away from the moving boundary. The shape of the shear profile is also determined by I, which is discussed in the next section.

[65] Some laboratory experiments have shown a discontinuous shear zone, with boundary shears near the moving wall at high stress and grain breakage [*Logan et al.*, 1979; 1992; *Mair et al.*, 2002] or distribution of shear across the layer. *Sazzard and Islam* [2008] present 2-D DEM in biaxial compression, with a decrease in the number of sliding contacts with increased particle friction consistent with our observations that high friction leads to jamming of the shear zone away from the moving boundary.

[66] If we move both upper and lower walls, effectively decreasing the shear zone thickness by a half, our profiles show a more distributed shear system because the number of sliding contacts has not decayed across the layer. Our simulations present the movement of only one wall for easier comparison to laboratory experiments, which only move one wall.

4.5. Role of Shear Strain and Velocity

[67] When the shear zone velocity is decreased in our simulations the curvature of the shear profiles decreases and the profile resembles continuous, distributed shear over the entire layer. *Shojaaee et al.* [2012a] show that the shape of the shear profile is dictated by the inertial number, I, (Equation (1)) in smooth wall simulations. As I decreases, and inertia becomes less important, profiles have less curvature and shear becomes distributed over the entire layer. The simulations of *Aharonov and Sparks* [2002] suggest that the behavior transition from the profiles presented in Figure 5 is reminiscent of a fluid to discontinuous profiles and shear banding near the boundary with increased pressure, or with decreased thickness. In the case of our simulations at $V_x = 1 \times 10^{-3}$, 2×10^{-4}, and 1×10^{-4} ($I \approx 4 \times 10^{-3}$, 2×10^{-4}, and 4×10^{-5}) for $R_{RMS} = 2.4$ and $\mu_{particle} = 0.5$, $\langle \mu_{macro} \rangle$ is indistinguishable within experiment uncertainty. At both $R_{RMS} = 0.35$ and $R_{RMS} = 0.58$ with $\mu_{particle} = 0.5$, and $V_x = 1 \times 10^{-3}$ or 2×10^{-4}, $\langle \mu_{macro} \rangle$ is equal within variability (Table 1). Simulations at $V_x = 1 \times 10^{-3}$ show no change in $\langle \mu_{macro} \rangle$ to $\gamma = 12$. Both *da Cruz et al.* [2005] and *Shojaaee et al.* [2012] find that $\langle \mu_{macro} \rangle$ increases with increasing I over many orders of magnitude, the velocity-strengthening situation.

4.6. Force and Fabric Network

[68] The trend of the force-probability relationship for the strong contact network, i.e., Figure 8, agrees with the

experiments of *Majmudar and Behringer* [2005] that shearing or weakly jammed systems show an exponential decay in the PDF. The value of β tends to follow shearing rate [*Behringer et al*., 2008] in 2-D systems. For the few 3-D simulations carried out, force distribution is consistent with an exponential, Equation (5) [*Silbet et al*., 2002a, 2002b; *Mair and Hazzard*, 2007]. The slope of the exponential has been shown to change slightly with tilt angle for particles sliding on a ramp, with interparticle forces to eight or more times the mean force [*Silbert et al*., 2002a, 2002b]. No systematic variation of β with R_{RMS} is present in our simulations, indicating the same probability density function describes the large force interactions for any roughness. We do find a slight dependence of β on $\mu_{\mathrm{particle}} < 0.5$.

[69] Simulations of shearing granular media in 3-D have shown the orientation of contacts at ~50° for 3-D simulations [*Mair and Hazzard*, 2007] for the high force contacts. In the 2-D simulations of *Aharonov and Sparks* [2004], high forces orient at ~45° with the orientation rotating during the stick-slip cycle. This rotation explains the large standard deviation observed in our contact orientation. As μ_{macro} varies during shear, the orientation of θ_s varies slightly from 48.5° to 50.5°. Even with the large standard deviation relative to the differences in measured contact orientation, there is a consistent increase of orientation with increased μ_{particle} for both $R_{\mathrm{RMS}} = 0.58$ and 2.4 (Figure 13). As μ_{particle} increases, the preferred orientation rotates closer to the normal direction. Additionally, low R_{RMS} models display higher $\langle\theta_s\rangle$ than high R_{RMS} models, as discussed in section 4.2. The trend of contacts aligning perpendicular to the shear direction with increasing μ_{particle} is in agreement with less overall contacts participating in shear at high μ_{particle}. Anisotropy of high force contacts has no clear trend with μ_{particle} due to the large standard deviation. As shown in Figure 14, anisotropy of the contact network does vary systematically with roughness. In all simulations the network of weak forces is nearly isotropic (Figure 13). Similar to the 3-D simulations of *Silbert et al*. [2002b], only a small variation in contact fabric is observed. The systematic trends of a and θ in Figure 13 are confirmed by the values of a and θ in Figure 14 with progressively decreasing roughness. In both cases, the values of a and θ are the result of the proportion of sliding versus locked contacts, with less sliding contacts promoting less anisotropy and a fabric network oriented closer to the shear normal direction.

[70] Systematic variations of both $\langle a_w\rangle$ and $\langle\theta_w\rangle$ exist even though the values of $\langle\theta_w\rangle$ have little meaning due to the isotropic nature of the weak contacts. Weak contacts do become slightly more anisotropic with increased μ_{particle} but in all cases, large numbers of grains contacts are present in all directions. The nearly isotropic weak contacts and extremely anisotropic strong contacts reflect which grains are sliding and which are locked and keeping the layer dilated. Strong contacts tend to align ~50° to the shear direction with few contacts at angles normal to shear or greater. This reflects that almost the entire strong contact network is locked and not sliding. If a large force were present and tangential to the grain contact, sliding would dissipate this force. Conversely grains participating in shear tend to be in the weak contact network. Because these particles are dilating and sliding over one another, contacts are present in all orientations.

[71] Other models have shown that the weak contact network can have a preferred orientation, particularly in stick-slip situations [*Aharonov and Sparks*, 2004]. *Aharonov and Sparks* [2004] proposed that the weak contact network buffers the strong contacts and force chains that resist shear. It is unclear if the difference in the weak contact network in our simulations is due to the lack of stick-slip or that our simulations are in 3-D and produce a more complicated network.

[72] Based on the idea that stick-slip sliding in granular media is the result of catastrophic buckling of force chains [e.g., *Morgan and Boettcher*, 1999], the high anisotropy and rotation of contact networks toward the shear direction indicate that simulations with rough boundaries could be less stable. The weak contact network is important in supporting strong contacts and force chains [e.g., *Aharonov and Sparks*, 2002; 2004]. In simulations where the weak network is dispersed at all orientations, the strong contact fabric could be unsupported leading to buckling [*Aharonov and Sparks*, 2002]. Our simulations do not present stick-slip due to the nearly infinite stiff loading system. With a three-dimensional shear zone, force chain networks are complex and promote stability.

4.7. Application to Natural Systems

[73] While our simulations are a vast simplification of any natural system without important components such as pore pressure, fluids, and grain shape, simulations do help elucidate the conditions that help lead to offset between the gouge and fault zone wall and how roughness helps to control the overall strength of a shear zone.

[74] Many natural systems include frictional sliding between a solid wall and granular shear zone, with offset between the wall-grains or deformation in the granular zone. Often natural systems include dissimilar materials in frictional contact. For example, large displacement faults often juxtapose different materials into contact. Glaciers can move by sliding of ice over the bed, or deformation within a till layer [*Cuffy and Paterson*, 2010] where dissimilar frictional materials are in contact with a low friction ice wall (which may or may not have debris entrained interacting with the particles beneath) and higher friction granular layer. Fault zones often contain a clay gouge zone, even in the presence of quartzo-feldspathic walls, a system of high friction walls and low friction particles [*Vrolijk and van der Pluijm*, 1999]. Finally, immature faults consist of fractured rocks producing wear material and gouge from the walls. In our simulations, when the roughness is large, a combination of wall roughness and grain friction controls behavior. As the roughness increases wall friction becomes more important.

[75] Natural fault zones often record displacement between the gouge zone and wall in the form of polished walls and other deformation markers. It has been proposed that a scaling break might be present with mature faults (i.e., faults with >10 m offset) showing less overall roughness than immature low total slip faults [*Sagy et al*., 2007; *Brodsky et al*., 2011]. While the idea that a break in the roughness scaling is not clearly observed for faults with larger accumulated slip [*Candela et al*., 2012], our results imply that a smooth fault could have less overall strength than a rough fault zone.

[76] The discrepancy between measurements of the critical slip distance in laboratory experiments and seismology has been attributed to the different roughness at the laboratory and fault scale [e.g., *Scholz*, 1998; *Biegel et al*., 1989; *Marone et al*., 1990]; however, the standard interpretation of the critical slip distance is the slip needed to renew the shearing contacts with the thickness of the shearing zone controlling the length scale [e.g., *Marone and Kilgore*, 1993; *Marone*, 1998; *Rathbun and Marone*, 2010]. This implies that roughness should only be important in cases where shear occurs between the boundary and gouge, or where roughness controls the thickness of the localized, active shearing zone. While our simulations consider stable sliding to investigate fault zone strength and as we do not investigate the transition from steady state sliding at one velocity to another, we do find that roughness and thus coupling of a fault to the gouge zones influences the number of sliding contacts, one of the factors that controls critical slip distance [*Marone and Kilgore*, 1993].

[77] In fast moving glaciers and ice streams, either sliding over a substrate composed of rock, or till; or deforming of the till layer is preferred to the creep, or regelation of ice. The roughness of the rock or till layer holds back the overriding ice sheet forcing ice to creep or regelate around bumps, both inherently slow processes. If the roughness of the glacial bed is low and ice slides, it may lack pinning points and lead to fast motion [*Kamb*, 1970]. Our simulations suggest that a glacier with a smooth bed would tend to slide over a basal till layer rather than deform that layer. In our simulations of low friction walls with high frictional particles, the situation most similar to glaciers, there is large offset at the wall-particle boundary and sliding is preferred to deformation of the layer.

5. Conclusion

[78] Three dimensional discrete element models on spherical particles sheared between rough ($R_{\mathrm{RMS}} >$ maximum grain size) or smooth walls ($R_{\mathrm{RMS}} <$ maximum grain size) accurately capture the behavior of laboratory experiments. The variation of fault zone strength with wall roughness and the frictional interactions between both fault gouge and fault zones walls is systematically investigated. The strength of the fault zone is controlled by both the frictional interactions and roughness. For both rough and smooth faults, shear strength of the fault zone increases with friction between particles with sensitivity to particle friction decreasing at high friction.

[79] For rough faults, the fault zone walls are coupled to the gouge zone, with only the gouge friction controlling strength. The wall and gouge are well coupled and any contrast of properties is unimportant. When large-scale roughness in the form of high amplitude grooves is removed and the fault zone is only rough at the particle scale, strength is controlled by a combination of wall friction, gouge friction and fine-scale roughness of the wall. In this case, strength is a linear function of roughness, with the friction coefficient controlling the intercept of the trend. Because the coupling of the wall is partially controlled by the friction of the wall, the contrast between wall and gouge properties plays a large role in determining the strength. Low wall friction promotes offset at the boundary between the gouge and wall and lower overall strength. High wall friction necessitates shearing of more gouge grains, requiring more stress to move the fault. For both smooth and rough fault models, the distribution of the particle-particle force obeys an exponential law above the mean particle force in the model. Grain contact orientation shows strong anisotropy in high force contacts at ~52° to the shear direction with the angle increasing with both particle-particle friction and roughness. Low force contacts are nearly isotropic in all cases.

[80] We suggest that the differences in strength are due to the thickness of the actively shearing zone and in particular, offset at the boundary. Rough faults force more deformation to occur in the fault zone, which requires more overall work to shear the fault. When the large roughness is removed, shear distribution is controlled by the difference between wall and gouge friction. These results imply that a smooth fault has a lower overall strength than rough fault if offset at the gouge-wall interface is possible. Strength differences are reflected in the macroscale measurement of shear zone thickness, and the correlation of shear zone thickness with model strength, coordination number, and finally the microscale controls of these values such as the number of sliding and locked grains, particle motion, and the manifestations of these, local porosity.

[81] **Acknowledgments.** We thank Dion Weatherley for help with ESyS-Particle and Behrooz Ferdowsi and Michele Griffa for assistance in fabric analysis. The project has been funded by the grant ANR-09-JCJC-0011-01. All of the computations presented in this paper were performed using the CIMENT infrastructure (https://ciment.ujf-grenoble.fr), which is supported by the Rhône-Alpes region (grant CPER07_13 CIRA: http://www.ci-ra.org). We thank Françoise Roch and Rodolphe Pinon for computing assistance. This manuscript benefited from discussions with Karen Mair and detailed reviews from an anonymous reviewer and Liran Goren.

References

Abe, S., D. Place, and P. Mora (2003), A parallel implementation of the lattice solid model for the simulation of rock mechanics and earthquake dynamics, *Pure Appl. Geophys*, *161*, 2265–2277.

Abe, S., and K. Mair (2009), Effects of gouge fragment shape on fault friction: New 3D modeling results, *Geophys. Res. Lett. 36*, L23302, doi:10.1029/2009GL040684.

Aharonov, E., and D. Sparks (1999), Rigidity phase transitions in granular packings, *Phys. Rev. E. 60*(6), 6890–6896.

Aharonov, E., and D. Sparks (2002), Shear profiles and localization in simulations of granular materials, *Phys. Rev. E. 65*, 302.

Aharonov, E., and D. Sparks (2004), Stick–slip motion in simulated granular layers, *J. Geophys. Res. 109*, B09306, doi:10.1029/2003JB002597.

Allen, M. P., and D. J. Tildesley (1987), *Computer Simulations of Liquids*, Clarendon Press, Oxford.

Angheluta, L., T. Candela, J. Mathiesen, and F. Renard (2011), Effect of surface morphology on the dissipation during shear and slip along a rock-rock interface that contains a visco-elastic core, *Pure Appl. Geophys. 168*(12), 2335–2344, doi:10.1007/s00024-011-0272-8.

Antonellini, M. A., and D. D. Pollard (1995), Distinct element modeling of deformation bands in sandstone, *J. Struct. Geol. 17*(8), 1165–1182.

Anthony, J., and C. Marone (2005), Influence of particle characteristics on granular friction, *J. Geophys. Res. 110*, B08409, doi:10.1029/2004JB003399.

Beeler, N. M., T. E. Tullis, M. L. Blanpied, and J. D. Weeks (1996), Frictional behavior of large displacement experimental faults, *J. Geophys. Res. 101*(B4), 8697–8715.

Behringer, R. P., K. E. Daniels, T. S. Mujmudar, and M. Sperl (2008), Fluctuations, correlations and transitions in granular materials: Statistical mechanics for a non-conventional system, *Phil. Trans. R. Soc. A. 366*, 493–504, doi:10.1098/rsta.2007.2106.

Biegel RL, Sammis CG, and Dieterich JH. (1989), The frictional properties of a simulated gouge with a fractal particle distribution. *J. Struct. Geol. 11*, 827–46.

Bistacchi, A., W. A. Griffith, S. A. F. Smith, G. Di Toro, R. Jones, and S. Nielsen (2011). Fault roughness at seismogenic depths from lidar and photogrammetric analysis, *Pure. Appl. Geophys. 168*(12), doi:10.1007/s00024-011-0301-7.

Bocquet, L., W. Losert, D. Schalk, T.C. Lubensky, and J.P. Gollub (2002), Granular shear flow dynamics and forces: Experiment and continuum theory, *Phys. Rev. E 65*(1), 1–19.

Bouchon, M, K. Karabulut, M. P. Bouin, J. Schmittbuhl, M. Vallee, R. Archuleta, S. Das, F. Renard, and D. Marsan (2010), Faulting characteristics of supershear earthquakes, *Tectonophys.*, *493*, 244–253, doi:10.1016/j.tecto.2010.06.011.

Boullier, A.-M., K. Fujimoto, T. Ohtani, G. Roman-Ross, E. Lewin, H. Ito, P. Pezard, and B. Ildefonse (2004), Textural evidence for recent co-seismic circulation of fluids in the Nojima fault zone, Awaji island, Japan, *Tectonophys.*, *378*, 165–181.

Bowden, F. P., and Tabor, D. (1950), *The Friction and Lubrication of Solids. Part I*. Oxford: Clarenden Press.

Brodsky, E. E., J. G. Gilchrist, A. Sagy and C. Colletini (2011), Faults smooth gradually as a function of slip, *Earth Planet Sci Lett.*, *302*, 185–193.

Burbridge, D. R., and J. Braun (2002), Numerical models of the evolution of accretionary wedges and fold-and-thrust belts using the distinct element method, *Geophys. J. Int. 148*(3), 542–561.

Candela, T., F. Renard, M. Bouchon, D. Marsan, J. Schmittbuhl, and C. Voisin (2009). Characterization of fault roughness at various scales: Implications of three-dimensional high resolution topography measurements, *Pure. Appl. Geophys.*, *166*, 1817–1851.

Candela, T., F. Renard, M. Bouchon, J. Schmittbuhl, and E.E. Brodsky (2011a), Stress drop during earthquakes: Effect of fault zone roughness scaling, *Bull. Seismological Soc. America 101*(5), 2369–2387.

Candela, T., F. Renard, M. Bouchon, J. Schmittbuhl, and E. E. Brodsky (2011b), Fault slip distribution and fault roughness, *Geophys. J. Int.*, *187*, 959–968, doi:10.1111/j.1365-246X.2011.05189.x.

Candela, T., F. Renard, Y. Klinger, K. Mair, J. Schmittbuhl, and E.E. Brodsky (2012), Roughness of fault surfaces over nine decades of length scales, *J. Geophys. Res.*, doi:10.1029/2011JB009041.

Cashman, S. M., and K. V. Cashman (2000), Cataclasis and deformation-band formation in unconsolidated marine terrace sand, Humboldt County, California, *Geology*, *28*, 111–114.

Cashman, S. M., J. N. Baldwin, K. V. Casman, K. Swanson, and R. Crawford (2007), Microstructures developed by coseismic and aseismic faulting in near-surface sediments, San Andreas Fault, California, *Geology*, *35*, 611–614.

Chester F. M., and J. S. Chester (1998), Ultracataclasite structure and friction processes of the Punchbowl Fault, San Andreas system, California, *Tectonophys.*, *295*, 199–221.

Chester, F. M., and J. S. Chester (2000), Stress and deformation along wavy frictional faults, *J. Geophys. Res.*, *105*, 23,421–23,430.

Chester, F. M., M. Friedman, and J. M. Logan (1985), Foliated cataclasites, *Tectonophys.*, *111*, 139–146.

Chester, F. M., and J. M. Logan (1986), Implications for mechanical properties of brittle faults from observations of the Punchbowl Fault Zone, California, *Pure Appl. Geophys.*, *124*, 79–106.

Choy, G. L., and S. H. Kirby (2004), Apparent stress, fault maturity and seismic hazard for normal-fault earthquakes at subduction zones, *Geophys. J. Int. 159*, 991–1012, doi:10.1111/j.1365-246X.2004.02449.x.

Cuffy, K. M., and W. S. B. Paterson (2010), *The Physics of Glaciers*, 4th Edition, Academic Press, Amsterdam, The Netherlands.

Cundall, P. A., and O. Strack (1979), A discrete numerical model for granular assembles, *Geotechnique*, *29*, 47–65.

da Cruz, F., Emam, S., Prochnow, M., Roux, J-N., and F. Chevoir (2005), Rheophysics of dense granular materials: Discrete simulation of plane shear flows. *Phys. Rev. E*, *72*, 021309.

Davies, T. R., M. J. McSaveney, and R. D. Beetham (2006), Rapid block glides: Slide-surface fragmentation in New Zealand's Waikaremoana landslide, *Quarterly J. Eng. Geol. and Hydrogeol.*, *39*(2), 115–129.

Davies, T., M. McSaveney, and K. Kelfoun (2010), Runout of the Socompa volcanic debris avalanche, Chile: A mechanical explanation for low basal shear resistance, *Bull. Volcanology*, *72*(8), 933–944, doi:10.1007/s00445-010-0372-9.

Dieterich, J. H., (1981) Constitutive properties of faults with simulated gouge, In *Mechanical Behavior of Crustal Rocks*, edited by N.L. Carter, M. Friedman, J. M. Logan, and D.W. Sterns, *24*, 103–120, AGU Monograph, AGU, Washington, D. C.

Dieterich, J. H., and D. E. Smith (2009). Nonplanar faults: Mechanics of slip and off-fault damage, *Pure and Applied Geophys.*, *166*, 1799–1815.

Faulkner, D. R., A. C. Lewis, and E. H. Rutter (2003), On the internal structure and mechanics of large strike-slip faults: field observations from the Carboneras fault, southeastern Spain, *Tectonophys.*, *367*, 235–251.

Finch, E. S. Hardy, and R. Gawthorpe (2003), Discrete element modeling of contractional fault-propagation folding above rigid basement fault blocks, *J. Struct. Geol. 25*(4), 515–528.

Fournier, T., and J. Morgan (2012), Insights to slip behavior on rough faults using discrete element modeling, *Geophys. Res. Lett.*, *39*, L12304, doi:10.1029/2012GL051899.

Frye, K. M., and C. Marone (2002), The effect of humidity on granular friction at room temperature, *J. Geophys. Res.*, *107*(11), 2309, doi:10.1029/2001JB000654.

Fulton, P. M., and A. P. Rathbun (2011), Experimental constraints on energy portioning during stick–slip and stable sliding within analog fault gouge, *Earth Planet. Sci Lett.*, *308*(2), 185–192, doi:10.1016/j.epsl.2011.05.051.

GDR Midi (2004), On dense granular flows, *Eur. Phys. J. E.*, *14*, 341–365, doi:10.1140/epje/i2003-10153-0.

Gee, M., R. Gawthorpe, and J. Friedmann (2005), Giant striations at the base of a submarine landslide. *Marine Geology*, *214*, 287–294.

Goren, L., E. Aharonov, D. Sparks, and R. Toussaint (2011), The mechanical coupling of fluid-filled granular material under shear, *Pure Appl. Geophys.*, 10.1007/s00024-011-0320-4.

Griffa, M., E. G. Daub, R. A. Guyer, P. A. Johnson, C. Marone, and J. Carmeliet (2011), Vibration-induced slip in sheared granular layers and the micromechanics of dynamic earthquake triggering, *Europhysics Lett.*, *96*, 10.1209/0295-5075/96/14001.

Hayman, N. W., B. A. Housen, T. T. Cladouhos, and K. Livi (2004), Magnetic and clast fabrics as measurements of grain-scale processes within the Death Valley shallow crustal detachment faults, *J. Geophys. Res.*, *109*, B05409, doi:10.1029/2003JB002902.

Hayward, I. P., I. L. Singer, and L.E. Seitzman (1992), Effect of roughness on the friction of diamond on CVD diamond coatings, *Wear*, *157*, 215–227.

Heermance, R., Z. K. Shipton, and J. P. Evans (2003), Fault structure control on the fault slip and ground motion during the 1999 rupture of the Chelungpu Fault, Taiwan, *Bull. Seismological Soc. Am. 93*(3), 1034–1050, doi:10.1785/0120010230.

Kamb, B. (1970), Sliding motion of glaciers: theory and observation, *Rev. of Geophys. and Space Phys.*, *8*(4), 673–728.

Kamb, B. (2001), Basal zone of the West Antarctic ice streams and its role in the lubrication of their rapid motion, in *The West Antarctic Ice Sheet: Behavior and Environment*, edited by R. B. Alley and R. A. Bindschadler, Antarctic Research Series, pp. 157–200, AGU, Washington, D. C.

Koval, G., J.-N. Roux, A. Corfdir, and F. Chevoir (2009), Annular shear of cohesionless granular materials: From the inertial to quasistatic regime, *Phys. Rev. E.*, *79*, 021306, doi:10.1103/PhysRevE.79.021306.

Knuth, M., and C. Marone (2007), Friction of sheared granular layers: Role of particle dimensionality, surface roughness, and material properties, *Geochem. Geophys. Geosyst.*, *8*, Q03012, doi:10.0129/2006GC001327.

Kruyt, N. P. (2003), Contact forces in anisotropic frictional materials, *Int. J. of Solids and Struct. 40*, 3537–3556.

Liu, C. H., S. R. Nigel, D. Schecter, S. N. Coppersmith, S. Majumadur, O. Narayan, and T. A. Witten (1995), Force fluctuations in bead packs, *Science*, *269*, 513–515.

Legros, F. (2002), The mobility of long-runout landslides, *Eng. Geol. 63*, 301–331.

Logan, J. M., C. A. Dengo, N. G. Higgs, and Z. Z. Wang (1992), Fabrics of experimental fault zones: Their development and relationship to mechanical behavior, in *Fault Mechanics and Transport Properties of Rocks*, edited by B. Evans and T. Wong, pp. 33–68, Academic Press, London.

Logan, J. M., M. Friedman, N. Higgs, C. Dengo, and T. Shimamodo (1979), Experimental studies of simulated fault gouges and their application to studies of natural fault zones, in *Analysis of Actual Fault Zones in Bedrock*, *US Geol. Surv. Open File Rep.*, *1239*, pp. 305–343.

Losert, W., L. Bocquet, T.C. Lubebsky, and J.P. Gollub (2000), Particle dynamics in sheared granular matter, *Phys. Rev. E*, *85*(7), 1428–1431.

Majmudar, T.S., and R.P. Behringer (2005), Contact force measurements and stress-induced anisotropy in granular materials, *Nature*, *435*, doi:10.1038/nature03805.

Makedonska, N., D. W. Sparks, E. Aharonov, and L. Goren (2011), Friction vs. dilation revisited: Insights from theoretical and numerical models, *J. Geophys. Res. 116*, B09302, doi:10.1029/2010JB008139

Marone, C. (1998), Laboratory-derived friction laws and their application to seismic faulting, *Ann. Revs., Earth Planet. Sci.*, *26*, 643–696.

Marone C., B. E. Hobbs, and A. Ord (1992), Coulomb constitutive laws for friction: Contrasts in frictional behavior for distributed and localized shear, *Pure and Applied Geophys.*, *139*, 195–214.

Marone, C., and B. Kilgore (1993), Scaling of the critical slip distance for seismic faulting with shear strain in fault zones. *Nature*, *362*, 618–621.

Marone, C., C. B. Raleigh, and C. H. Scholz (1990), Frictional behavior and constitutive modeling of simulated fault gouge, *J. Geophys. Res.*, *95*(B5), 7007–7025.

Mair, K., and S. Abe (2008), 3D numerical simulations of fault gouge evolution during shear: Grain size reduction and strain localization, *Earth Planet. Sci. Lett*, *274*, 72–81.

Mair, K., K. M. Frye and C. Marone (2002), Influence of grain characteristics on the friction of granular shear zones, *J. Geophys. Res. 107*(10), 2219, doi:10.1029/2001JB000516.

Mair, K., and J. F. Hazzard (2007), Nature of stress accommodation in sheared granular material: insights from 3D numerical modeling, *Earth Planet. Sci. Lett. 30*, 469–485, doi:10.1016/j.epsl.2007.05.006.
Mora, P., and D. Place (1994), Simulation of the frictional stick–slip instability, *Pure Appl. Geophys*, *143*, 61–87.
Mora, P., and D. Place (1998), Numerical simulation of earthquake faults with gouge: Towards a comprehensive explanation for the heat flow paradox, *J. Geophys. Res.*, *103*, 21,067–21,089.
Morgan, J. K. (1999), Numerical simulations of granular shear zones using the distinct element method, 1. Shear zone kinematics and the micromechanics of localization, *J. Geophys. Res.*, *104*(B2), 2,703–2,718.
Morgan, J. K., and M. S. Boettcher (1999), Numerical simulations of granular shear zones using the distinct element method: Shear zone kinematics and micromechanics, *J. Geophys. Res.*, *104*, 2703 – 2719.
Morgan, J. K., and P. J. McGovern (2005a), Discrete element simulations of gravitational volcanic deformation: 1. Deformation structures and geometries, *J. Geophys. Res. 110*, B05402, doi 10.1029/2004JB003252.
Morgan, J. K., and P. J. McGovern (2005b), Discrete element simulations of gravitational volcanic deformation: 2. Mechanical analysis, *J. Geophys. Res. 110*, B05403, doi 10.1029/2004JB003253.
Mueth, D. M, G. F. Debregeas, G.S. Karczmar, P.J. Eng, S. Nagel, and M. Jaeger (2000), Signatures of granular microstructure in dense shear flows, *Nature*, *406*, 385–389.
Mühlhaus, H. B., and Vardoulakis, I. (1987), The thickness of shear bands in granular materials, *Geotechnique*, *37*, 271–283.
Nye, J. F. (1969), The calculation of sliding of ice over a wavy surface using a Newtonian viscous approximation, *Proceedings of the Royal Society, London*, *A311*(1506), 445–467.
Pechmann, J. C., and H. Kanamori (1982), Waveforms and spectra of preshocks and aftershocks of the 1979 Imperial Valley, California, earthquake: Evidence for fault heterogeneity?, *J. Geophys. Res.*, *87* (B13), 10,579–10,597, doi:10.1029/JB087iB13p10579.
Persson, B. N. J. (1998), *Sliding Friction, Physical Principles and Applications*, 2nd ed., Springer-Verlag, Kluwer, Germany.
Place, D., and P. Mora (1999), The lattice solid model: Incorporation of intrinsic friction, *J. Int. Comp. Phys.*, *150*, 332–372.
Place, D., and P. Mora (2001), A random lattice solid model for simulation of fault zone dynamics and fracture processes, in *Bifurcation and Localization, Theory for Soils and Rocks*, edited by H. B. Mühlhaus, A. V. Dyskin, and E. Pasternak, pp. 321–333, A. A. Balkema, Brookfield, Vt.
Pöschel, T., and T. Schwager (2005), *Computation Granular Dynamics: Models and Algorithms*, Springer Press, Berlin, Heidelberg.
Pouliquen, O., and R. Gutfraind (1996), Stress fluctuations and shear zones in quasistatic granular chute flows, *Phys. Rev. E*, *53*(1), 552–561.
Power, W. L., T. E. Tullis, S. R. Brown, G. N. Boitnott, and C. H. Scholz (1987). Roughness of natural fault surfaces, *Geophys. Res. Lett. 14*, 29–32.
Power, W. L., T. E. Tullis, and J. D. Weeks (1988). Roughness and wear during brittle faulting, *J. Geophys. Res. 93*, 15268–15278, doi:10.1029/JB093iB12p15268.
Radjaï, F., and F. Dubois (2011), *Discrete-Element Modeling of Granular Materials*, Wiley, Hoboken, N.J.
Radjaï, F., J. Michel, J.-J. Moreau, and S. Roux (1996), Force distributions in dense two-dimensional granular systems, *Phys. Rev. Lett.*, *77*(2), 274–277.
Radjaï, F., D. E. Wolf, M. Jean, and J.-J. Moreau (1998), Bimodal character of stress transmission in granular packings, *Phys. Rev. Lett.*, *80*(1), 61–64.
Rathbun, A. P., C. Marone, R. B. Alley, and S. Anandakrishnan (2008), Laboratory study of the frictional rheology of sheared till, *J. Geophys. Res.*, *113*, F02020, doi:10.1029/2007JF000815.
Rathbun, A. P., and C. Marone (2010), Effect of strain localization on frictional behavior of granular materials, *J. Geophys. Res.*, *115*, B01204, doi:10.1029/2009JB006466.
Renard, F., C. Voisin, D. Marsan, and J. Schmittbuhl (2006). High resolution 3D laser scanner measurements of a strike-slip fault quantify its morphological anisotropy at all scales, *Geophys. Res. Lett. 33*, L04305, doi:10.1029/2005GL025038.
Rosakis, A. J., O. Samudrala, and D. Coker (1999), Cracks faster than the shear wave speed, *Science*, *284*, 1337–1340.
Ross, N., R. G. Bingham, H. F. J. Corr, F. Ferraccioli, T. A. Jordan, A. Le Brocq, D. M. Rippin, D. Young, D. D. Blankenship, and M. J. Siegert (2012), Steep reverse bed slope at the grounding line of the Weddell Sea sector in West Antarctica, *Nature Geosci. 5*, 393–396, doi:10.1038/ngeo1468.
Rothenburg, L., and R. J. Bathurst (1989), Analytical study of induced anisotropy in idealized granular materials, *Géotechnique 39*(4), 601–614.
Roux, J. N., and F. Chevior (2011), Dimensional analysis and control parameters, in *Discrete-Element Modeling of Granular Materials*, edited by F. Radjaï and F. Dubois, Wiley, Hoboken, N.J.
Sagy A., E. E. Brodsky, and G. J. Axen (2007). Evolution of fault-surface roughness with slip, *Geology*, *35*, 283–286.
Saltzer, S. D., and D. D. Pollard (1992), Distinct element modeling of structures formed in sedimentary overburden by extensional reactivation of basement normal faults. *Tectonics 11*(1): doi: 10.1029/91TC02462.
Sammis, C. G., and S. J. Steacy (1994), The micromechanics of friction in a granular layer, *Pure Applied Geophys*, *143*, 777–794.
Saucier, F., E. Humphreys, and R. Weldon (1992), Stress near geometrically complex stick-slip faults—Application to the San Andreas Fault at Cajon Pass, Southern California, *J. Geophys. Res.*, *94*(B4), 5081–5094, doi:10.1029/91JB02644.
Sazzard, Md. M., and Md. S. Islam (2008), Macro and micro mechanical responses of granular material under varying interparticle friction, *J.Civil Engineering*, *36*(2), 87–96.
Schmittbuhl, J., G. Chambon, A. Hansen, and M. Bouchon (2006), Are stress distributions along faults the signature of asperity squeeze? *Geophys. Res. Lett. 33*, L13307, doi:10.1029/2006GL025952.
Scholz, C.H. (1998). The critical slip distance for seismic faulting, *Nature 336*, 761–763.
Scholz, C. H. (2002), *The Mechanics of Earthquakes and Faulting*, 2nd ed., Cambridge Univ. Press, New York.
Schubnel, A., S. Nielsen, J. Taddeucci, S. Vinciguerra, and S. Rao (2011), Photo-acoustic study of subshear and supershear ruptures in the laboratory, *Earth Planet. Sci. Lett. 308*, 424–432.
Shojaaee, Z, J.-N. Roux, F. Chevoir, and D. E. Wolf (2012a), Shear flow of dense granular materials near smooth walls. I. Shear localization and constitutive laws in the boundary region, *Phys. Rev. E*, *86*, 011301, doi:10.1103/PhysRevE.86.011301.
Shojaaee, Z. L. Brendel, J. Török, and D.E. Wolf (2012b), Shear flow of dense granular materials near smooth walls. II. Block formation and suppression of slip by rolling friction, *Phys. Rev. E*, *86*, 011302, doi:10.1103/PhysRevE.86.011302.
Sibson, R. H. (1977), Fault rocks and fault mechanisms, *J. Geol. Soc. London*, *133*, 191–214.
Sibson, R. H. (1984), Roughness at the base of the seismogenic zone: Contributing factors, *J. Geophys. Res.*, *89*, 5791–5799.
Silbert, L. E., D. Ertas, G. S. Grest, T. C., and D. Levine (2002a), Analogies between granular jamming and the liquid-glass transition, *Phys. Rev. E*, *65*, 051307.
Silbert, L. E., G. S. Grest, and J. W. Landry (2002b), Statistics of the contact network in frictional and frictionless granular packings, *Phys. Rev. E*, *66*, 061303.
Tsai, J.-C., and J. P. Gollub (2005), Granular packings sheared in an annular channel: Flow localization and grain size dependence, *Phys. Rev E*, *72*, 051304, doi:10.1103/PhysRevE.72.051304.
van der Elst, N. J., E. E. Brodsky, P._Y. Le Bas, and P. A. Johnson (2012), Auto-acoustic compaction in steady shear flows: Experimental evidence for suppression of shear dilatancy by internal acoustic vibration, *J. Geophys. Res.*, *117*, B09314, doi:10.1029/2011JB008897.
Veje, C. T., D. W. Howell, and R. P. Behringer (1999), Kinematics of two-dimensional granular Couette experiment at the transition to shearing, *Phys. Rev. E*, *59*(1), 739–745.
Venkataraman, A., and H. Kanamori (2004). Observational constraints on the fracture energy of subduction zone earthquake, *J. Geophys. Res.*, *109*, B05302, doi:10.1029/2003JB002549.
Vrolijk, P., and B. A. van der Pluijm (1999), Clay gouge, *J. Struct. Geol.*, *21*, 1039–1048.
Walsh, S. D. C., A. Tordesillas, and J. F. Peters (2007), Development of micromechanical models for granular media, *Granular Matter*, *9*, 337–352, doi:10.1007/s10035-007-0043-5.
Wang, Y., Abe, S., Latham, S., and P. Mora (2006), Implementation of particle–scale rotation in the 3-D lattice solid model. *Pure Applied Geophys. 163*, 1769–1785.
Xia, K., A. J. Rosakis, and H. Kanamori (2004), The sub-Rayleigh-to-supershear rupture transition, *Science*, *303*(5665), 1859–1861.
Zoback, M., S. Hickman, and W. Ellsworth (2010), Scientific drilling into the San Andreas fault zone, *EOS Trans. AGU 91*(22), 197–199.